



## JRC TECHNICAL REPORT

# Experimental validation of the TAF-ID: High temperature behaviour of simulated Ex-vessel corium and MOX-Lanthanides (Ce, Gd, La, Nd)

JRC in-kind contribution to the TAF-ID Stage 2 Project

Geiger, E.; Benes, O.; Vigier, J.-F.; Boboridis, K.;  
Robba, D.; Colle, J.-Y.; Cremer, B.; Ernstberger, M.;  
Pöml, P.; Himbert, J.; Gardeur, S.; Lajarge, P.;  
Popa, K.; Boshoven, J.; Vlahovic, L.; Wiss, T.;  
Piro, M.H.A.; Konings, R.J.M.

2023

This publication is a Technical report by the Joint Research Centre (JRC), the European Commission's science and knowledge service. It aims to provide evidence-based scientific support to the European policymaking process. The contents of this publication do not necessarily reflect the position or opinion of the European Commission. Neither the European Commission nor any person acting on behalf of the Commission is responsible for the use that might be made of this publication. For information on the methodology and quality underlying the data used in this publication for which the source is neither Eurostat nor other Commission services, users should contact the referenced source. The designations employed and the presentation of material on the maps do not imply the expression of any opinion whatsoever on the part of the European Union concerning the legal status of any country, territory, city or area or of its authorities, or concerning the delimitation of its frontiers or boundaries.

**Contact information**

Name: Ondrej Benes

Address: European Commission, Joint Research Centre, Karlsruhe, Germany

Email: [ondrej.benes@ec.europa.eu](mailto:ondrej.benes@ec.europa.eu)

Tel.: +49 7247 951 385

**EU Science Hub**

<https://joint-research-centre.ec.europa.eu>

JRC135045

EUR 31715 EN

PDF ISBN 978-92-68-08691-9

ISSN 1831-9424

doi:10.2760/693912 KJ-NA-31-715-EN-N

Luxembourg: Publications Office of the European Union, 2023

© European Atomic Energy Community, 2023



The reuse policy of the European Commission documents is implemented by the Commission Decision 2011/833/EU of 12 December 2011 on the reuse of Commission documents (OJ L 330, 14.12.2011, p. 39). Unless otherwise noted, the reuse of this document is authorised under the Creative Commons Attribution 4.0 International (CC BY 4.0) licence (<https://creativecommons.org/licenses/by/4.0/>). This means that reuse is allowed provided appropriate credit is given and any changes are indicated.

For any use or reproduction of photos or other material that is not owned by the European Atomic Energy Community permission must be sought directly from the copyright holders.

How to cite this report: Geiger, E.; Benes, O.; Vigier J.-F.; Boboridis, K.; Robba D.; Colle J.-Y.; Cremer B.; Ernstberger M.; Pöml P.; Himbert J.; Gardeur S.; Lajarge P.; Popa K.; Boshoven J.; Vlahovic L.; Wiss T.; Piro M.H.A.; Konings R.J.M., *Experimental validation of the TAF-ID: High temperature behaviour of simulated Ex-vessel corium and MOX-Lanthanides (Ce, Gd, La, Nd)*, Publications Office of the European Union, Luxembourg, 2023, doi:10.2760/693912, JRC135045.

# Experimental validation of the TAF-ID: High temperature behaviour of simulated Ex-vessel corium and MOX-Lanthanides (Ce, Gd, La, Nd)

E. Geiger<sup>a,b</sup>, O. Beneš<sup>a</sup>, J-F. Vigier<sup>a</sup>, K. Boboridis<sup>a</sup>, D. Robba<sup>a</sup>, J-Y. Colle<sup>a</sup>, B. Cremer<sup>a</sup>, M. Ernstberger<sup>a</sup>, P. Pöml<sup>a</sup>, J. Himbert<sup>a</sup>, S. Gardeur<sup>a</sup>, P. Lajarge<sup>a</sup>, K. Popa<sup>a</sup>, J. Boshoven<sup>a</sup>, L. Vlahovic<sup>a</sup>, T. Wiss<sup>a</sup>, M.H.A Piro<sup>b</sup>, R.J.M. Konings<sup>a</sup>

<sup>a</sup>European Commission, Joint Research Centre, Karlsruhe, 76125, Germany

<sup>b</sup>Department of Energy and Nuclear Engineering, Ontario Tech University, 2000 Simcoe St N, Oshawa, L1G 0C5, ON, Canada

---

## Abstract

Two systems were investigated at the Joint Research Centre (JRC)-Karlsruhe for the experimental validation of the Thermodynamic of Advanced fuels - International Database (TAF-ID). The first system was representative of ex-vessel corium, consisting of nuclear fuel, fuel cladding, steel, and concrete representative materials, while the second consisted of  $(\text{U}, \text{Pu})\text{O}_2$  (MOX) with lanthanides (2.5 at.% each of Ce, Gd, La, and Nd). Experimental observations included laser heating, for measuring liquidus and solidus temperatures; SEM-EDS, EPMA, and XRD for characterising the fuel microstructure, phases composition, and crystal structure; and KEMS, for measuring the vapour pressure of species. The obtained results were compared to thermodynamic calculations using the TAF-ID. Excellent agreement was observed between experimental and calculated results in the  $\text{UO}_2$ -corium system, particularly of the liquidus and solidus temperatures, and the composition of phases. Results obtained on the MOX-corium system were not fully conclusive due to some experimental challenges. They do suggest, however, that some thermodynamic models should be reviewed, particularly those of U-Zr-O and U-Pu-Zr-O in the hypo-stoichiometric region. Regarding the MOX-Lanthanides system, evidence of silicon contamination was observed that led to the formation of a Si-, Pu-, and lanthanide-rich phase in a ratio consistent with  $\text{M}_2\text{SiO}_4$ . Although significant differences were observed between experimental results and thermodynamic calculations due to this contamination, the miscibility gap in the system has been confirmed experimentally. In addition, this contamination has allowed identifying important knowledge gaps in the database, which will lead to continued improvements.

---

## 1. Introduction

The Thermodynamic of Advanced Fuels - International Database (TAF-ID) project has developed an internationally recognized thermodynamic database for nuclear materials that will assist in the development of Gen IV reactors and contribute to lifetime extension, safety improvement, and safety analysis for Gen II & III systems. The current version of the database, v.15, contains thermodynamic models for 237 binary and 109 ternary systems. These binary and ternary assessments can be extrapolated for calculations of higher order systems, but experimental validation on such systems is mandatory to ensure the accuracy of the models and identify knowledge gaps. With the latter objective, two multi-component systems have been studied at the Joint Research Centre (JRC) - Karlsruhe: Ex-vessel corium and Mixed Oxides - Lanthanides (MOX-Ln). Ex-vessel corium is a complex mixture of materials that may be formed during late stages of

nuclear accidents, when the reactor core has melted and discharged onto the concrete base following the failure of the reactor vessel. Thus, ex-vessel corium may consist of molten irradiated nuclear fuel and its cladding, steel from structural materials, control rods, concrete, etc. Furthermore, depending on the severe accident scenario (succession of events that lead to the formation of ex-vessel corium), these components may experience a different degree of oxidation as they interact with H<sub>2</sub>O (steam), H<sub>2</sub>, or even O<sub>2</sub> (air). Accurately predicting the chemical behaviour of ex-vessel corium is of utmost importance as the information generated by thermodynamic calculations can be used in severe accident codes to improve their predictions.

The interest on the MOX-Ln system lies in the need of improving the understanding of MOX nuclear fuel behaviour during irradiation. Indeed, the incorporation of lanthanide fission products into the fluorite lattice of the nuclear fuel could induce miscibility gaps, thus modifying the fuel microstructure and material properties, such as thermal conductivity. Experimental observation on such multi-component systems is challenging, as some chemical elements can interfere with others thereby reducing the accuracy of measurements. This is particularly important in techniques involving X-rays such as Scanning Electron Microscopy - Energy Dispersive X-ray Spectroscopy (SEM-EDS), Electron-Probe Micro Analysis (EPMA), or X-Ray Diffraction (XRD), but also in mass-spectrometry techniques such as Knudsen Mass Effusion Spectroscopy (KEMS). Then, it is important for systems to be as simple as possible while remaining representative of real systems, so that the uncertainty of experimental measurements is minimized and the accuracy required for validating the TAF-ID can be achieved. Therefore, the composition of each system has been limited to include only representative species: Ex-vessel corium samples studied in this work consist of UO<sub>2</sub> and PuO<sub>2</sub>, representative of the nuclear fuel; Zr/ZrO<sub>2</sub>, representative of the fuel cladding; Fe/Fe<sub>2</sub>O<sub>3</sub>, representative of structural materials; and CaO/SiO<sub>2</sub> representative of concrete. On the other hand, MOX-Ln samples consist of (U, Pu)O<sub>2</sub> with four lanthanides: Ce, Gd, La, and Nd.

The experimental techniques employed for studying these systems are laser heating, for determining the solidus and liquidus temperatures; SEM-EDS, EPMA, and XRD for identifying the phases and determining their composition before and after laser experiments; and lastly KEMS, for measuring the vapour pressure of species with respect to temperature. This report is organized in the following sections: Sample preparation procedure for both systems and the description of the experimental techniques and conditions are presented in section 2; Experimental results and thermodynamic calculations of ex-vessel corium samples are presented in section 3, while those on the MOX-Ln system are presented in section 4. Lastly, conclusions and recommendations are presented in section 5 and References in section 6.

## 2. Materials and Methods

The samples composition and preparation procedure is presented first, followed by a description of the techniques and experimental set-ups used for their characterization. These techniques are (i) Laser Heating, for the determination of liquidus and solidus temperatures, (ii) SEM-EDS and EPMA, for the characterisation of samples microstructure and phases chemical composition, (iii) XRD, for the identification of crystal structures, and (iv) KEMS, for measuring the vapour pressure of species.

## 2.1. Samples preparation

### 2.1.1. Ex-vessel corium

As mentioned, the samples studied in this work are representative of ex-vessel corium and consist of the following species: UO<sub>2</sub> and PuO<sub>2</sub> (representing the nuclear fuel), Zr and ZrO<sub>2</sub> (fuel cladding), Fe and Fe<sub>2</sub>O<sub>3</sub> (steel, structural materials), and SiO<sub>2</sub> and CaO (concrete). Following discussions with colleagues from Japan Atomic Energy Agency (JAEA) [1], the ratio of materials was set to (in mass) 56.2% nuclear fuel, 18.8% cladding, 10.0 % steel, and 15.0% concrete. A generic accident scenario was considered for defining the ratio of species, being the main intention to have oxide and metallic phases coexist. Therefore, the metal-to-oxide mass ratio of cladding and steel components was set to 1, as well as the mass ratio of concrete species. Regarding the nuclear fuel, a 9:1 mass ratio UO<sub>2</sub>/PuO<sub>2</sub> was considered. Two different batches were prepared: with and without plutonium, but maintaining the ratio of other components. Hence, these two systems are further referred to as UO<sub>2</sub>-corium and MOX-corium henceforth. The nominal composition of samples is presented in Table 1.

Sample preparation was as follows: First, the corresponding amounts of depleted UO<sub>2</sub>, ZrO<sub>2</sub>, SiO<sub>2</sub>, and CaCO<sub>3</sub> were mixed and calcined at 800 °C under flowing Ar + 4% H<sub>2</sub> in a conventional resistance furnace, in order to bring UO<sub>2</sub> close to stoichiometry and to decompose CaCO<sub>3</sub> into CaO. Corresponding amounts of Fe, Zr, and Fe<sub>2</sub>O<sub>3</sub> were then added, and the mixture was separated into two batches: one that constituted the UO<sub>2</sub>-corium batch, and a second to which PuO<sub>2</sub> (high purity, less than 0.1 wt.% Am) was added, constituting the MOX-corium batch. Lastly, the two batches were pressed into pellets (6.5 mm diameter, 3.0 mm high) and sintered at 1600 °C for 4 hours under flowing Ar + 4% H<sub>2</sub>. However, due to technical problems, the sintering time of the UO<sub>2</sub>-corium batch was only of 1.5 hours.

Table 1: Nominal composition of UO<sub>2</sub>- and MOX-corium samples

Species	Composition (wt.%)	
	UO <sub>2</sub> -corium	MOX-corium
UO <sub>2</sub>	53.60	50.60
PuO <sub>2</sub>	0.00	5.60
Zr	9.96	9.40
ZrO <sub>2</sub>	9.96	9.40
Fe	5.30	5.00
Fe <sub>2</sub> O <sub>3</sub>	5.30	5.00
SiO <sub>2</sub>	7.94	7.50
CaO	7.94	7.50

### 2.1.2. MOX-lanthanides

MOX samples containing 2.5 at.% each of Ce, Gd, La, and Nd were prepared using the gel supported co-precipitation method. Their composition is given in Table 2. Two batches were prepared, with different oxygen to metal (O/M) ratios: 2.00 and 1.97. The former was used as a reference, and the latter was the batch of interest. These batches were prepared with the following procedure:

- $\text{La}(\text{NO}_3)_3 \cdot 6\text{H}_2\text{O}$ ,  $\text{Ce}(\text{NO}_3)_3 \cdot 6\text{H}_2\text{O}$ ,  $\text{Nd}(\text{NO}_3)_3 \cdot 6\text{H}_2\text{O}$ , and  $\text{Gd}(\text{NO}_3)_3 \cdot 6\text{H}_2\text{O}$  starting powders were dissolved in a  $\text{HNO}_3$  solution, and mixed with a 2 M  $\text{UO}_2(\text{NO}_3)_2$  solution, considering the target ratio of elements.
- $\text{PuO}_2$  powder was dissolved in a 12 M  $\text{HNO}_3$ , 0.1 M HF solution under active stirring and heated to reflux during 24 hours, to produce a solution containing 0.5 M  $\text{Pu}^{4+}$ . Both solutions were mixed together.
- After adding Methocel A4C (methyl cellulose polymer, to increase viscosity) and Triton X-100 (surfactant), the solution was dropped in a 6 M  $\text{NH}_3$  solution to induce the hydrolysis and co-precipitation of actinides and lanthanides.
- The resulting beads were filtered, dried, and calcined first at 800 °C under air to eliminate remnants of organic compounds, followed by a second calcination under  $\text{Ar}/\text{H}_2$  for 6 hours to bring the metals close to their final oxidation state.
- 5 g of powder were produced and pressed into discs of about 400 mg each at 500 MPa. 5 pellets were sintered at 1600 °C under  $\text{Ar}/\text{H}_2(4\%)/\text{H}_2\text{O}$  (1000 ppm) to obtain stoichiometric material ( $\text{O/M} = 2$ ), while the remainder were sintered also at 1600 °C but under a dry  $\text{Ar}/\text{H}_2(4\%)$  to obtain hypo-stoichiometric material. However, the target temperature could not be maintained for the initially planned 4 hours due to a furnace malfunction, and samples were cooled down naturally to room temperature right after reaching 1600 °C.
- Thermogravimetric analysis determined that the O/M ratio of the hypo-stoichiometric batch was 1.97.

As the interest of this system lies mainly with hypo-stoichiometric material, unless otherwise specified MOX-Ln refers only to the hypo-stoichiometric batch further in the text.

Table 2: Nominal composition of MOX-Ln samples.

<b>Species</b>	<b>Composition (at.%)</b>
$\text{UO}_2$	72.0
$\text{PuO}_2$	18.0
$\text{CeO}_{1.5}$	2.5
$\text{GdO}_{1.5}$	2.5
$\text{LaO}_{1.5}$	2.5
$\text{NdO}_{1.5}$	2.5

## 2.2. Laser Heating

The Laser Heating instrument at JRC-KA, its calibration, and operation are described in detail by Manara *et al.* [2]. Only the salient characteristics are recalled here. The instrument essentially consists of a chamber, two lasers, a pyrometer, and a spectrometer. Samples are secured in graphite sample holders, which are placed inside the chamber. The latter is a cylindrical vessel with sapphire windows (optical transmittance = 0.855) on each side that can be operated at a maximum over-pressure of 0.5 MPa. The chamber is located inside an inert-atmosphere glovebox, on which there is also a Suprasil window (optical transmittance = 0.933). A high-power Nd:YAG laser (4500 W; wavelength,  $\lambda$  = 1064 nm) is used for heating the samples. The beam is usually focused to a 3 mm spot on the sample surface. A second low-power Ar<sup>+</sup> laser (0.75 W,  $\lambda$  = 488 nm) is used for monitoring changes in the reflectivity of the samples' surface. This Reflected Light Signal (RLS) assists in the determination of state transition temperatures: a constant signal indicates a solid surface, while oscillations indicate liquid state (due to surface tension-induced vibrations) or solid-solid phase transitions. The sample temperature and the RLS are recorded using a two-channel fast pyrometer, tuned at 650 nm (sample temperature) and 488 nm (RLS). A 256-channel radiance spectro-pyrometer is used mainly for determining the samples emissivity, which is later used to calculate the surface temperature. Lastly, the O<sub>2</sub> partial pressure ( $P_{O_2}$ ) at the inlet and outlet of the chamber is monitored using zirconia sensors (MicroPoas). One of the main advantages of this experimental set-up is that it allows measuring phase transition temperatures with the sample acting as its own crucible, preventing possible interactions with foreign materials.

A typical laser sequence in UO<sub>2</sub> and MOX-corium experiments consisted of three stages: a first low-power laser pulse (30 W, 1 s) to increase the sample temperature up to about 2100 K, a high-power laser pulse (100 W, 0.3 s) up to about 3200 K during which the sample is melted, and lastly a cooldown period to room temperature. The pre-heating stage is meant to reduce the thermal stress produced by intense thermal gradients, and avoid the mechanical failure and subsequent destruction of the sample [3]. The data recorded during the last stage is of interest for the determination of liquidus and solidus temperatures. Each sequence was repeated five times for repeatability purposes, letting the  $P_{O_2}$  return to initial values between sequences. As mentioned, the emissivity of samples during the first thermal arrest after the high-power pulse was determined by the spectrometer. This emissivity, along with the transmissivity of chamber and glovebox windows, was used to re-calculate the temperature reading by the fast pyrometer. The data processing method is described by Manara *et al.* [2]. Representative results obtained with this technique are presented in Figure 1, illustrating what has been described so far.

## 2.3. Scanning Electron Microscopy - Electron-Dispersive X-ray Spectroscopy (SEM-EDS)

As-sintered and post-laser heated samples of UO<sub>2</sub>- and MOX-corium were cut along their longitudinal section (at approximately the centre of the laser-melted region), embedded in epoxy resin, and polished using different disks and solutions from 30 to 1  $\mu$ m grit. Samples were then analyzed in a Phillips XL 40 SEM coupled with an EDAX EDS detector. Since EDS quantitative analysis is not particularly sensitive to light elements, such as oxygen, all species were considered as stoichiometric. This consideration resulted in an increased confidence on the measured content of heavy and light elements, but did not allow determining different oxidation states of a same element. Therefore, the most stable oxidized state was considered for all

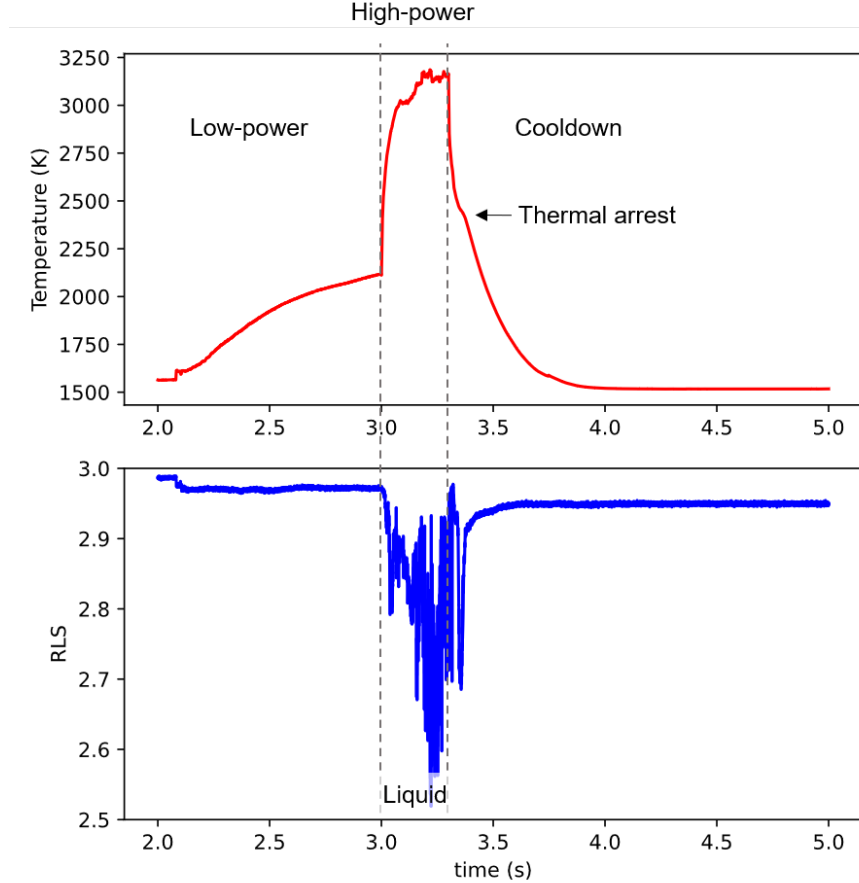


Figure 1: Thermogram and Reflected-Light Signal (RLS) acquired during 1<sup>st</sup> laser shot on a UO<sub>2</sub>-corium sample. Only the cooldown section is considered for analysis.

elements present in phases that consisted clearly of oxides, but Fe and Si in metallic state were considered for metallic phases.

#### 2.4. Electron Probe - Micro Analysis (EPMA)

EPMA characterisation was conducted only on MOX-Ln samples. The instrument is a Cameca SXR 100, installed in an enclosure specially shielded and modified to permit the analysis of irradiated nuclear fuels. It is equipped with four wavelength dispersive spectrometers, two of which have quartz 10̄11 monochromators that facilitate the analysis of actinides. Samples were embedded in epoxy resin, polished down to 1 µm diamond paste, and coated with a 20 nm conductive Al film to avoid charging effects. Reference materials (UO<sub>2</sub> for U, PuO<sub>2</sub> for Pu, LaPO<sub>4</sub> for La, CePO<sub>4</sub> for Ce, NdPO<sub>4</sub> for Nd, Gd for Gd, and SiO<sub>2</sub> for Si) were coated with an Al layer of the same thickness to avoid the necessity of correction of the film. Intensities were acquired for U M $\alpha$  and Pu M $\alpha$  using quartz monochromators, for the lanthanides L $\alpha$  lines using a LiF monochromator, and for Si K $\alpha$  using a TAP monochromator. The instrument was set to an electron acceleration potential of 25 kV and a beam current of 100 nA for the samples and 20 nA for the reference materials. Matrix effects were corrected using the PAP model [4]. Mass absorption coefficients (MACs) were

taken from the work of Farthing and Walker [5], whereas the MACs for O K $\alpha$  were taken from that of Pöml and Llovet [6]. Counting times were 20 s (peak) and 2 x 10 s (background) on the reference materials and 30 s (peak) and 2 x 15 s (background) on the sample.

### 2.5. X-ray Diffraction (XRD)

XRD measurements were performed using a Bruker D8 Advance diffractometer (Cu K $\alpha$  radiation, 40 kV, 40 mA) with a Bragg-Brentano  $\theta/2\theta$  configuration, equipped with a curved Ge monochromator (111) and a Lynxeye linear position-sensitive detector. Diffraction patterns were recorded at room temperature across an angular range  $20^\circ \leq 2\theta \leq 110^\circ$ , with at 0.013 angular step. XRD analysis was conducted on as-sintered corium and MOX-Ln samples. Data was treated with the software MAUD, with the sole purpose of identifying the crystal structures. A full Rietveld analysis or phase fraction determination was not possible due to a significant difference in the relative intensity of experimental data to the reference materials. This difference is linked to a preferred orientation of crystals, caused both by the small amount of materials that was recovered from the samples and the sample holder being static with respect to the incident X-ray beam.

### 2.6. Knudsen Effusion Mass Spectrometry (KEMS)

The KEMS experimental setup at JRC-Karlsruhe is thoroughly described in literature by Smith *et al.* [7], only the main characteristics are mentioned here. The instrument, located entirely in a shielded glovebox, consists of a Knudsen effusion cell coupled to a quadrupole mass spectrometer QMG422 (Pfeiffer Vacuum GmbH). The Knudsen cell is placed in a high temperature furnace heated by tungsten-coil heating elements. The furnace is placed in a high vacuum chamber ( $10^{-5}$  to  $10^{-6}$  mbar). The mass spectrometer covers the range of 1 to 512 amu. Experiments were conducted at a constant electron ionization energy of 32.85 eV, up to 2437 K. Tungsten crucibles were employed, which are chemically inert to oxide fuel samples and allow a complete vaporization. KEMS characterisation was performed on the MOX-corium and MOX-Ln systems. An additional observation was carried out on pure ZrO<sub>2</sub> in order to determine the ionization potential of these species for the analysis of MOX-corium results. A fixed amount of Ag was placed in the crucibles along with the samples for calibration purposes, which is a standard practice in this technique [7]. The obtained KEMS data were corrected considering the appearance potential curve of species.

## 3. Ex-vessel corium samples

### 3.1. Experimental Results

#### 3.1.1. Laser Heating experiments

Laser Heating experiments were conducted on UO<sub>2</sub>- and MOX-corium samples, using the experimental sequence described in Section 2.2 (three stages: low power pulse, high power pulse, and cooldown). Results acquired on UO<sub>2</sub>-corium samples are presented first, followed by those on MOX-corium. For each system, the thermograms obtained during the first and fifth laser shots are compared to illustrate the evolution of their behaviour. The recorded oxygen partial pressure down-stream the chamber is presented last. In this technique, the liquidus and solidus temperatures are usually determined considering the beginning and end of the thermal arrests on the recorded thermograms, respectively. Then, the liquidus and solidus correspond to the slope changes on the thermogram and are observed directly or can be identified on its first derivative.

In addition, the solidus and liquidus should also match features on the RLS [2, 8]. However, the beginning of the thermal arrest was not always clean due to, for instance, the high cooling rate after the high-power laser pulse (approximately 9000 K/s, as observed in these experiments) and the volatilization of species at high temperature. A consequence of the former is a rather “flat” thermal arrest, with a plateau at about the solidus temperature [9], and of the latter the presence of oscillations on the RLS that are still observed during the liquid-to-solid transition. These and other limitations are elaborated further for each system in the text. Lastly, as mentioned previously, the emissivity of the samples during each test was obtained from the spectrometer recorded data and specifically at the temperature plateau of the thermal arrest. This emissivity was then considered constant with temperature and used to recalculate the pyrometer temperature. This is of course a simplification, as the emissivity of a body is a function of temperature and wavelength. Nevertheless, the total error in these measurements, taking into account the uncertainty associated with the pyrometer calibration, emissivity, transmittance of the optical system, *etc.*, is lower than  $\pm 2\%$  of the reported temperatures [10].

### **UO<sub>2</sub>-corium**

The thermogram, its first derivative, and RLS data recorded during the cooldown period after the first and fifth laser shot on a UO<sub>2</sub>-corium sample are presented in Figure 2 (a) and (b), respectively. The thermal arrest observed on the thermogram corresponds to the liquid-to-solid phase transition. The RLS data clearly indicates this transition: during the high-power laser section and up to 3.32 s, the oscillations on the RLS signal are attributed to the light-scattering effect of a turbulent liquid surface. The smooth signal observed thereafter mark the beginning of solidification. The solidus temperature,  $T_S$ , correlates with by the slope change on the first derivative of the thermogram, which corresponds to the minimum of the RLS signal. Two features,  $T'$  and  $T_L$ , are observed on the thermogram and its first derivative before the temperature plateau in Figure 2 and could correspond to the liquidus temperature. However,  $T'$  is located in a region on the RLS with many oscillations, while  $T_L$  marks the beginning of a pronounced change in the RLS behaviour. The latter feature is then considered to be indicative of the beginning of solidification of the molten material,  $T_L$ . The measured  $T_L$  and  $T_S$  values over the five laser shots on this sample are presented in Table 3, along with the sample emissivity considered for each shot. The average measured values are  $T_L = 2610 \pm 10$  K, and  $T_S = 2443 \pm 5$  K. As observed, these values and particularly those of the liquidus showed a tendency to decrease with successive laser shots. In addition, it was observed that the time at which these features occurred increased with each cycle, while the intensity of the features (particularly that of  $T'$ ) decreased with successive shots. The latter can be observed in Figure 2 (b), in which the results of the first and fifth shot are compared. As observed, all the features  $T'$ ,  $T_L$ , and  $T_S$  are shifted to a later time from the first to the fifth shot. A hypothesis on the nature of the  $T'$  feature is that it is related to the volatilization of material at high temperature. This would explain why the oscillations on the RLS region where this feature is observed decrease with successive shots (visible on the comparison of the RLS signals on Figure 3 (B)): volatile compounds being released from the molten materials would produce perturbations on its surface (and therefore oscillations on the RLS signal), that would decrease with successive shots as more and more volatiles are released. Further experimentation would be required to confirm this hypothesis, at a pressure high enough to suppress the formation of the gas phase.

### **MOX-corium**

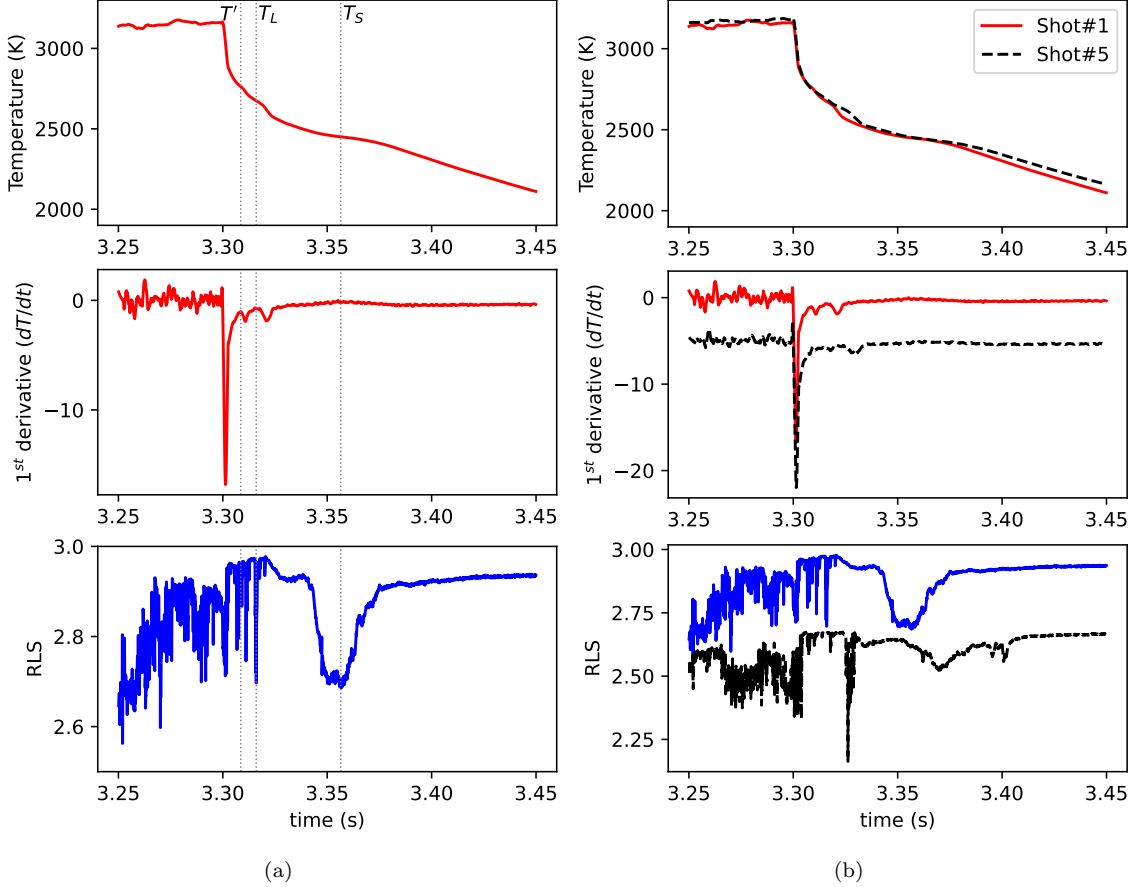


Figure 2: Laser heating results acquired on a UO<sub>2</sub>-corium sample. Thermogram, its 1<sup>st</sup> derivative, and RLS signal acquired during the 1<sup>st</sup> laser shot (a), compared to results acquired during the 5<sup>th</sup> shot (b).  $T_L$  indicates the liquidus temperature, which marks the beginning of a profound change on the RLS signal.  $T_S$  indicates the solidus temperature, associated to the end of the thermal arrest.

The thermogram, its first derivative, and RLS data, recorded during the cooldown period after the first and fifth laser shot on a MOX-corium sample, are presented in Figure 3 (a) and (b), respectively. As already mentioned, the thermal arrest is associated with a liquid-solid phase transition, being the liquidus and solidus temperatures the beginning and end of the arrest, respectively.

Although the solidus temperature ( $T_S$ ) can be easily identified on the thermogram, the liquidus temperature ( $T_L$ ) is not as evident as the cooldown behaviour of this sample is different to that of the UO<sub>2</sub>-corium sample: the shape of the thermal arrest (almost flat) would indicate a phase transition at a rather constant temperature, and the features on the thermogram before the thermal arrest are weak. In addition, many oscillations are present on the RLS signal even during the solidification of the material. As with UO<sub>2</sub>-corium experiments, a hypothesis for this behaviour is the volatilization of material at high temperature, which is supported by the decrease in the frequency and intensity of oscillations on the RLS with successive laser shots on the sample (Figure 3 (b)). This hypothesis is further elaborated with the aid of thermodynamic calculations in Figure 3.2. For consistency, the liquidus temperature in MOX-corium experiments has been

Table 3: Liquidus ( $T_L$ ) and Solidus ( $T_S$ ) temperatures measured on a UO<sub>2</sub>-corium sample during laser heating experiments. Experimental uncertainty:  $\pm 20K$

	<b>Emissivity</b>	<b>T<sub>L</sub> (K)</b>	<b>T<sub>S</sub> (K)</b>
Shot#1	0.73	2675	2450
Shot#2	0.73	2632	2446
Shot#3	0.72	2598	2444
Shot#4	0.73	2636	2440
Shot#5	0.72	2622	2433
Average	0.73	$2633 \pm 18$	$2443 \pm 5$

determined following the same approach for UO<sub>2</sub>-corium ones, by taking the temperature at which a major change in the behaviour of the RLS signal is observed. The measured liquidus and solidus temperatures are summarized in Table 4, although it must be kept in mind that there is a high uncertainty in the measured values of the liquidus temperature. Further experimentation would be required, particularly at a pressure high enough to suppress the formation of the gas phase, for a more accurate determination of the liquidus temperature. Despite this limitation, the average solidus temperature determined for this samples is  $2684 \pm 5$  K, **241 K higher than that of UO<sub>2</sub>-corium samples**. The contrast between the behaviour of both systems is better observed in Figure 4, where the thermograms recorded during the first laser cycle of each sample are superimposed.

Table 4: Liquidus ( $T_L$ ) and Solidus ( $T_S$ ) temperatures measured on a MOX-corium sample during laser heating experiments.

	<b>Emissivity</b>	<b>T<sub>L</sub> (K)</b>	<b>T<sub>S</sub> (K)</b>
Shot#1	0.68	2720	2687
Shot#2	0.68	2774	2691
Shot#3	0.68	2737	2686
Shot#4	0.69	2731	2680
Shot#5	0.69	2792	2675
Average	0.68	$2751 \pm 26$	$2684 \pm 5$

### Oxidation of samples during laser experiments

The oxygen partial pressure ( $P_{O_2}$ ) was monitored downstream from the chamber to determine whether samples were oxidized during laser heating experiments. The recorded data vs. time for each laser shot on both systems (UO<sub>2</sub>- and MOX-corium) are presented in Figure 5 (a) and (b), respectively. In both

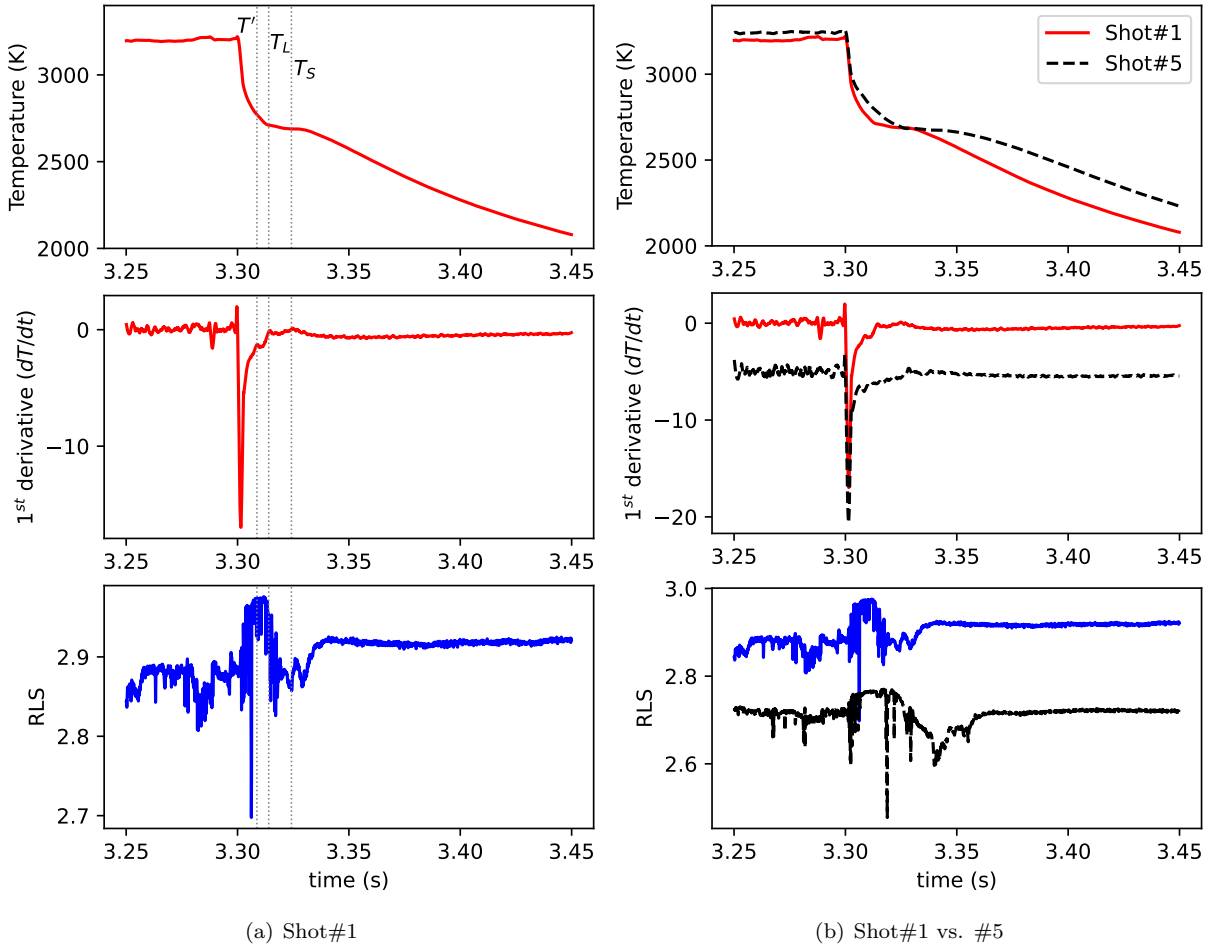


Figure 3: Left: Thermogram, its 1<sup>st</sup> derivative, and RLS signal acquired during the 1<sup>st</sup> laser shot on a MOX-corium sample. The solidus,  $T_S$ , corresponds to the temperature plateau. The liquidus could correspond to the feature observed on the 1<sup>st</sup> derivative indicated by  $T'$ , but both the thermogram and RLS signal do not offer any particular support. Right: Comparison of results acquired during the 1<sup>st</sup> and 5<sup>th</sup> laser sequences on the same sample. Although  $T_S$  remains similar, all the different features observed in the three diagrams shift to higher time with successive laser sequences. The 1<sup>st</sup> derivative and RLS data for Shot#5 are shifted vertically for easy of comparison.

cases, the  $P_{O_2}$  decrease is attributed to the consumption of oxygen by the samples at high temperature. Although both systems consumed O<sub>2</sub> from the carrier gas, their behaviour is not identical: The oxygen consumption of the MOX-corium sample was highest during the first laser shot, decreasing with successive heating sequences, while the oxygen consumption for the UO<sub>2</sub>-corium sample was similar during the first and fifth (last) shot. A system evolving towards chemical equilibrium would consume less and less O<sub>2</sub> after each heating sequence. However, at least two other phenomena that take place simultaneously must be considered: (i) the composition of the systems evolves during each heating sequence as volatile species are released, which may oxidize as they are released, and (ii) the transport of species (oxygen inwards but volatile and phases with a density lower than that of the matrix outwards). Then, the reduction in oxygen consumption can be attributed to the system moving towards chemical equilibrium, but also to a reduction

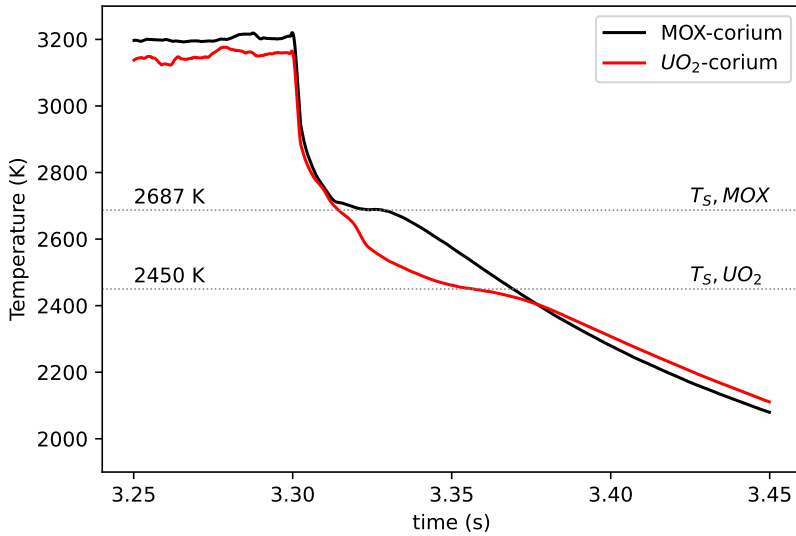


Figure 4: Thermograms recorded during the 1<sup>st</sup> laser sequence on a UO<sub>2</sub>-corium (red) and MOX-corium (black) samples. The solidus temperature,  $T_S$ , of the MOX-corium sample is considerably higher than that of the UO<sub>2</sub>-corium one.

of the amount of material susceptible of being oxidized (notably Si and Fe) and transport limitations.

### 3.1.2. SEM-EDS

SEM-EDS characterisation was completed on as-sintered and post-laser heating experiments of UO<sub>2</sub>- and MOX-corium samples. Results of UO<sub>2</sub>-corium samples are presented first, followed by MOX samples. As mentioned in section 2, X-Ray techniques such as SEM-EDS have a limited sensitivity to light elements, such as oxygen. To compensate for this limitation, the oxygen content was not measured directly in these measurements but estimated considering the stoichiometric compounds SiO<sub>2</sub>, CaO, ZrO<sub>2</sub>, Fe<sub>2</sub>O<sub>3</sub>, and UO<sub>2</sub> for phases that were clearly constituted by oxides, and Fe, Si, CaO, ZrO<sub>2</sub>, and UO<sub>2</sub> for metallic ones.

### UO<sub>2</sub>-corium

The cross-section image of a UO<sub>2</sub>-corium sample submitted to five laser shots is presented in Figure 6. Regions A and B of the latter correspond to regions that were melted by the laser. The hourglass shape of the sample is a consequence of the sintering step (densification of the material) rather than the loss of material during laser experiments. Regions C and D correspond to as-sintered and melted material, respectively, on which elemental X-ray mapping and quantitative composition analyses were performed. These results are presented next.

#### As-sintered region

A SEM-SE image acquired in the as-sintered region of a UO<sub>2</sub>-corium sample is presented in Figure 7 (a), along with X-ray maps of Fe (b), Ca (c), Si (d), U (e), and Zr (f). These X-ray maps are greyscale-coded: the brighter, the higher the concentration of the probed element. As oxygen is a light element and X-ray techniques are not sensitive enough, the X-ray map of this element is not presented here to

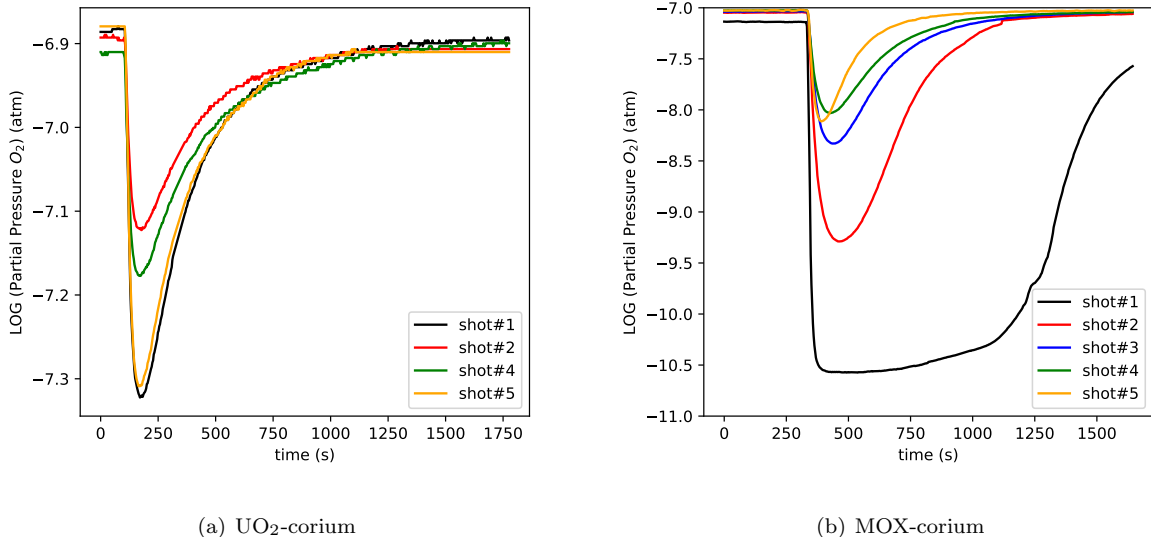


Figure 5:  $O_2$  partial pressure monitored downstream the chamber during laser heating experiments.

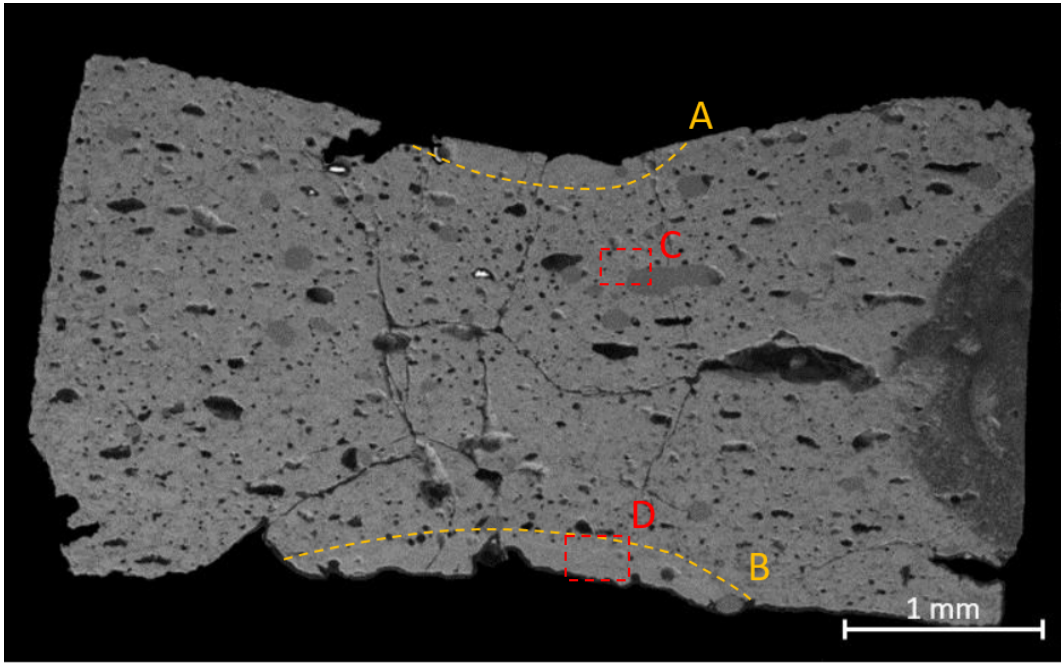


Figure 6: Cross-section of a  $UO_2$ -corium sample.

avoid misinterpretations. These results indicate that at least four different phases are present, each with a distinctive microstructure: (i) two fluorite phases,  $(U, Zr)O_{2\pm x}\#1$  and  $\#2$ , (ii) a Ca- and Si- rich oxide phase denoted as  $CaSiO_x$ , and (iii) a metallic Fe-rich phase denoted as  $\alpha$ -Fe. The measured composition of these phases is presented in Figure 8. Despite the mentioned limitations of this technique and the likely interference from neighbouring phases (due to the small size of the probed phases), no significant

differences in composition were observed for a same phase across the sample. The main observations from these measurements are summarized as follows:

- (i) The fluorite phases present different U/Zr ratios and microstructure:  $(U, Zr)O_{2\pm x}\#1$  presents a U/Zr ratio  $\approx 4.5$  and very small grains (points 1 and 2 in Figure 8), while  $(U, Zr)O_{2\pm x}\#2$  presents a U/Zr ratio  $\approx 0.9$  and larger grains (points 3 and 4 in Figure 8). These distribution likely indicates a miscibility gap in the fluorite phase. Given the small grain size of the  $(U, Zr)O_{2\pm x}\#1$  phase, the measured content of Si and Ca is most likely a contribution of the surrounding  $CaSiO_X$  phase.
- (ii) According to SEM-EDS quantitative results, the oxygen to metal ratio (O/M) of fluorites #1 and #2 are approximately 1.75 and 1.85, respectively. Although such a low O/M is very unlikely (again, attributed to the low sensitivity of X-ray techniques to light elements such as oxygen), these results suggest that both fluorite phases are hypo-stoichiometric.
- (iii) The composition of the oxide phase rich in Ca and Si was measured in points 5 and 6 in Figure 8. The ratio of these elements is consistent with  $CaSiO_3$  (Si/O molar ratio = 1:3).
- (iv) The metallic phase (points 7 and 8 in Figure 8), consists of Fe (99.3 at.%) with traces of Si (0.6 at.%). XRD characterisation indicates that this phase has BCC crystal structure, which is consistent with  $\alpha$ -Fe.

#### Laser-melted region

A SEM-SE image acquired in the melted region of a  $UO_2$ -corium sample is presented in Figure 9 (a), along with X-ray maps of elements Fe (b), Ca (c), Si (d), U (e), and Zr (f). This image and X-ray maps were acquired on region D, highlighted in Figure 6: the periphery of the sample corresponds to the bottom of the image, and the boundary of the melted region is indicated by the dashed line. Beyond this boundary, the microstructure of the sample is still different to that of as-sintered material. This is likely a consequence of the high temperature to which this region was submitted, causing the material to re-sinter or promoting a limited transport of species. Three main phases can be identified from these results: (i) a single fluorite,  $(U, Zr)O_{2\pm x}$ , (ii) a Si-Ca rich oxide phase, and (iii) a Fe-rich metallic phase. The composition of these phases is presented in Figure 10. Again, it must be kept in mind that quantitative results are mostly indicative: the size and distribution of phases can lead to a considerable interference and overlapping of results (*e.g.*, the high content of Si, Ca, and Fe in the fluorite phase is likely a contribution from surrounding phases). The main observations are summarized below:

- (i) The microstructure of the melted region is substantially different to that of the as-sintered material, with dendrites of Si and Ca rich oxides surrounding globular grains of fluorite. The growth direction of these grains suggest that the melted material closer to the bulk of the sample solidified towards the periphery, but that the material at the periphery solidified towards the bulk.
- (ii) Three main phases are identified: a fluorite phase,  $(U, Zr)O_{2\pm x}$ ; a metallic Fe-rich phase,  $\alpha$ -Fe; and a  $CaSiO_X$  phase. The latter could be similar to the  $CaSiO_3$  phase observed in the as-sintered region.
- (iii) No indication of a miscibility gap in the fluorite phase is observed either in the U and Zr X-ray maps or in the SE image (microstructure). The fluorite phase,  $(U, Zr)O_{2\pm x}$ , presents an average O/M=1.75.

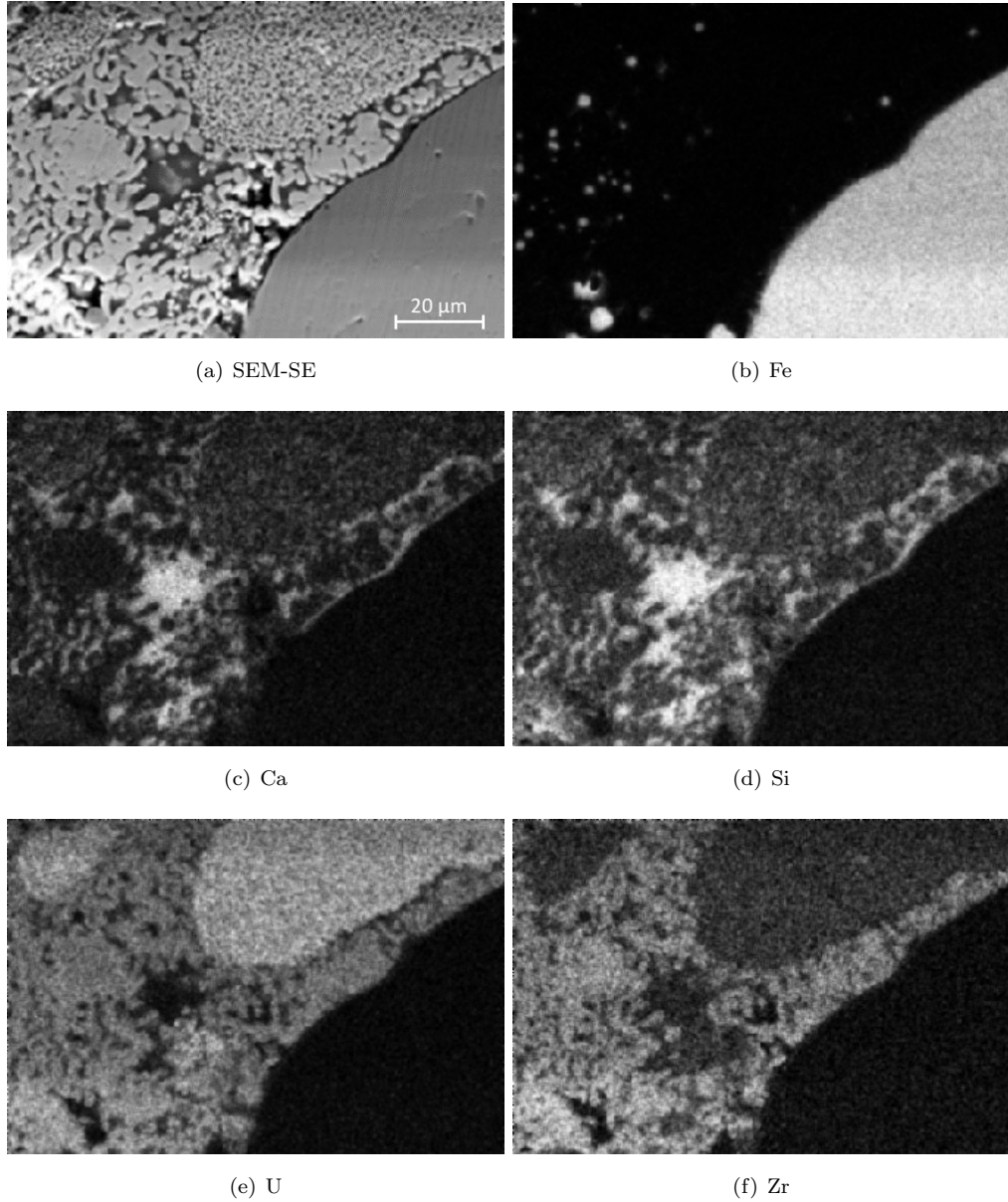
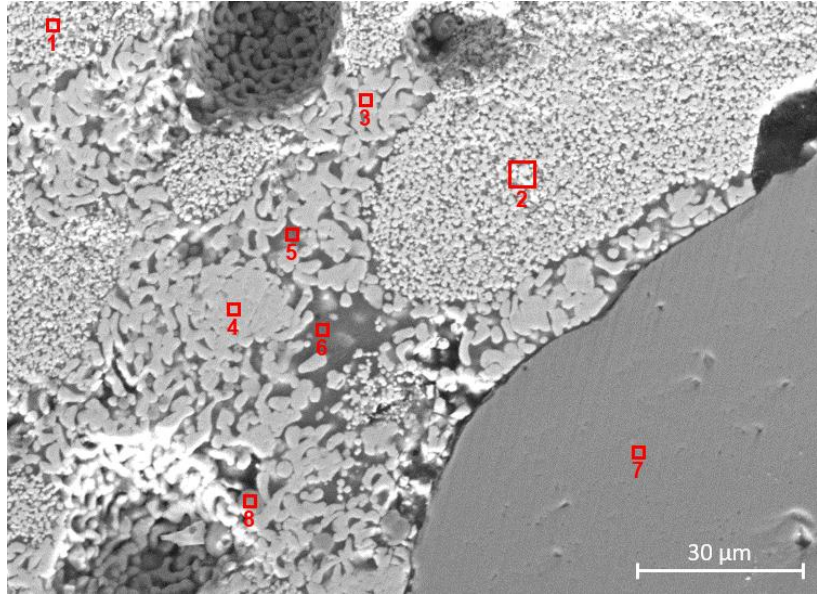


Figure 7: Fe, Ca, Si, U, and Zr X-ray maps acquired on an as-sintered UO<sub>2</sub>-corium sample.

- (iv) The size and number of Fe-rich precipitates decreases in the melted region towards the periphery of the sample, while the Fe concentration in the dendrites (CaSiO<sub>X</sub> phase) increases. This Fe concentration gradient is explicit in quantitative points 5, 6, and 7 on Figure 10, where the measured Fe concentration in the CaSiO<sub>X</sub> phase is 6.3, 10.6, and 13.1 at.% Fe, respectively. This suggests that Fe was oxidized during the laser heating experiments.
- (v) The Si concentration in the CaSiO<sub>X</sub> phase is lower in the melted region than in the as-sintered material: The Si/Ca ratio in the as-sintered material is 1.25, while in the melted region it is 0.85. This suggests



Phase	Point	Composition (at.%)					
		O	Si	Ca	Fe	Zr	U
$(\text{U}, \text{Zr})\text{O}_2\#1$	1	63.6	14.1	8.7	0.4	2.6	10.5
	2	63.7	14.2	8.4	0.5	2.2	11.1
$(\text{U}, \text{Zr})\text{O}_2\#2$	3	64.9	9.3	4.5	0.8	10.6	9.9
	4	65.2	8.8	4.0	0.5	11.9	9.7
$\text{CaSiO}_X$	5	61.0	18.6	14.5	2.6	1.7	1.7
	6	60.8	20.3	16.8	0.7	0.9	0.5
$\alpha\text{-Fe}$	7	0.1	0.6	0.0	99.3	0.0	0.0
	8	0.1	0.6	0.0	99.3	0.0	0.0

Figure 8: Quantitative characterisation of an as-sintered  $\text{UO}_2$ -corium sample.

that Si was partially released during the laser heating experiments.

### MOX-corium

The cross-section image of a MOX-corium sample submitted to laser heating experiments is presented in Figure 11. The regions denoted A and B on the latter correspond to regions that were melted by laser. MOX-corium samples do not exhibit the hourglass shape observed in  $\text{UO}_2$ -corium samples due to densification during sintering. Regions C and D correspond to as-sintered and melted material, respectively, on which elemental X-ray mapping and quantitative composition analyses were performed. These results are presented next.

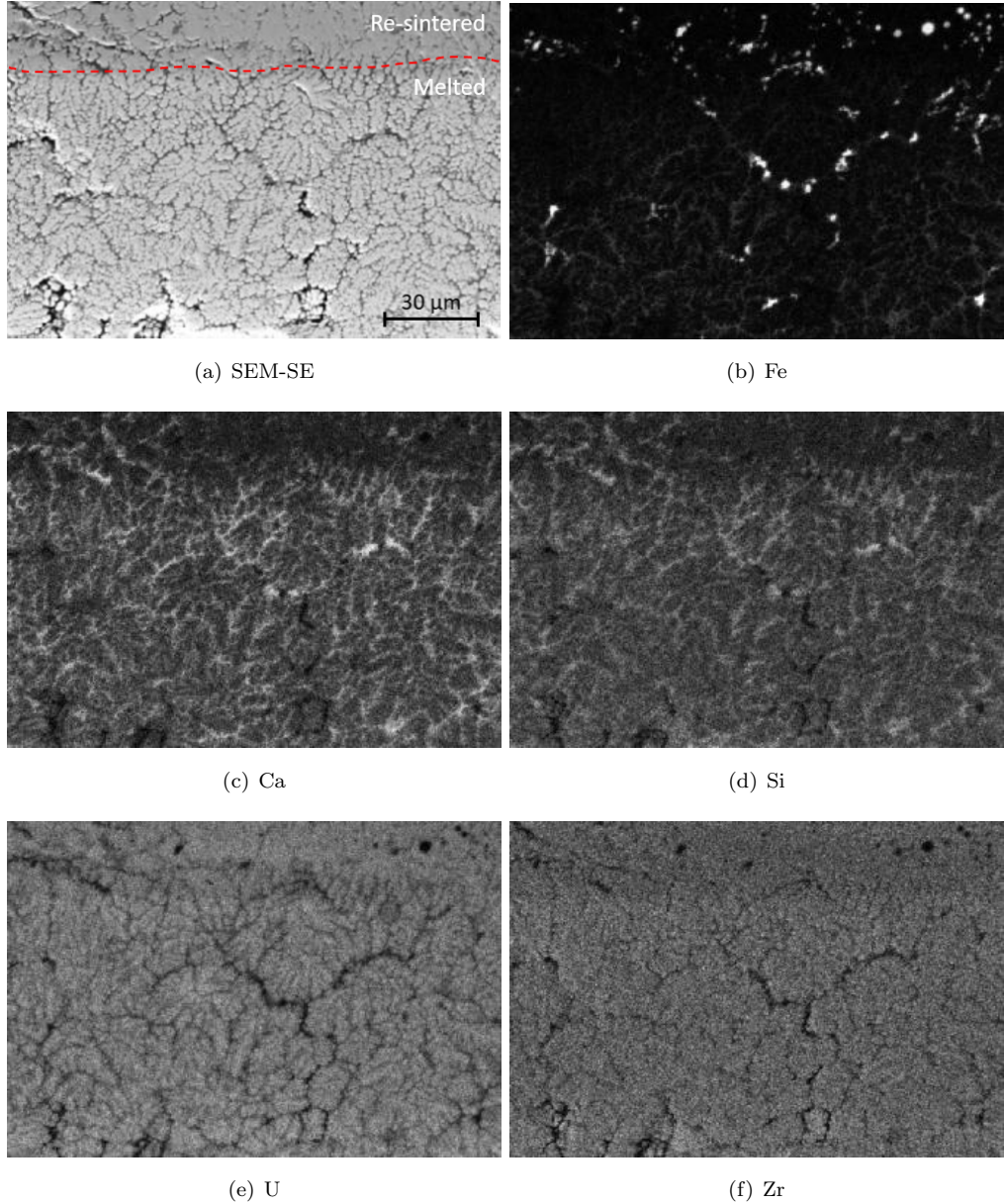
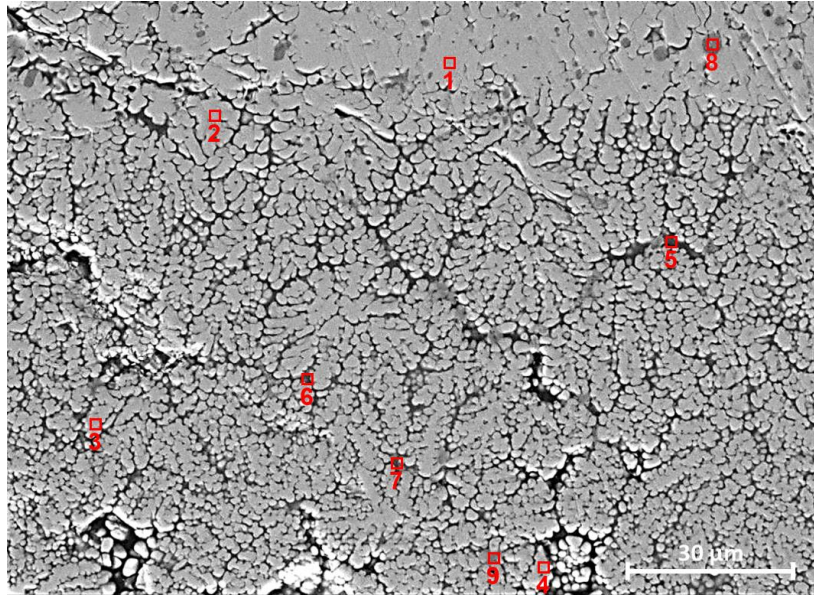


Figure 9: Fe, Ca, Si, U, and Zr X-ray maps acquired on the laser-melted region of a  $\text{UO}_2$ -corium sample.

#### As-sintered region

A SEM-SE image acquired in the as-sintered region of a MOX-corium sample is presented in Figure 12 (a), along with X-ray maps of elements Fe (b), Ca (c), Si (d), U (e), Pu (f), and Zr (g). Three main phases can be identified from these results: (i) a single fluorite,  $(\text{U}, \text{Pu}, \text{Zr})\text{O}_{2\pm x}$ , (ii) a Si- and Ca- rich oxide phase ( $\text{CaSiO}_X$ ), and (iii) a Si- and Fe-rich metallic phase ( $\alpha$ -Fe). The composition of these phases is presented in Figure 13. Again, it must be kept in mind that quantitative results must be taken with caution as the size and distribution of phases can lead to a considerable interference and overlapping of results. Experimental



Phase	Point	Composition (at.%)					
		O	Si	Ca	Fe	Zr	U
$(\text{U}, \text{Zr})\text{O}_2$	1	64.8	8.6	4.3	1.2	6.6	14.6
	2	63.3	7.4	4.7	5.4	6.1	13.1
	3	62.8	9.5	8.0	3.6	5.7	10.4
	4	63.7	6.8	7.2	1.7	8.1	12.5
$\text{CaSiO}_X$	5	58.8	13.3	17.4	6.3	1.9	2.4
	6	58.7	12.0	13.4	10.6	2.4	3.0
	7	58.2	11.1	12.5	13.1	2.3	3.0
$\alpha\text{-Fe}$	8	0.2	0.7	0.0	99.1	0.0	0.1
	9	7.7	1.9	1.4	85.8	1.5	1.6

Figure 10: Quantitative characterisation of the laser-melted region of a  $\text{UO}_2$ -Corium sample.

observations are summarized below.

- (i) A single fluorite phase,  $(\text{U}, \text{Pu}, \text{Zr})\text{O}_{2\pm X}$ , is observed in the as-sintered region of MOX-corium samples: No signs of a miscibility gap are observed in both the sample microstructure and on the U, Pu, and Zr X-ray maps in Figure 12.
- (ii) The average O/M ratio of the fluorite phase is 1.88, although such a low value is unlikely and attributed to the accuracy of the technique.

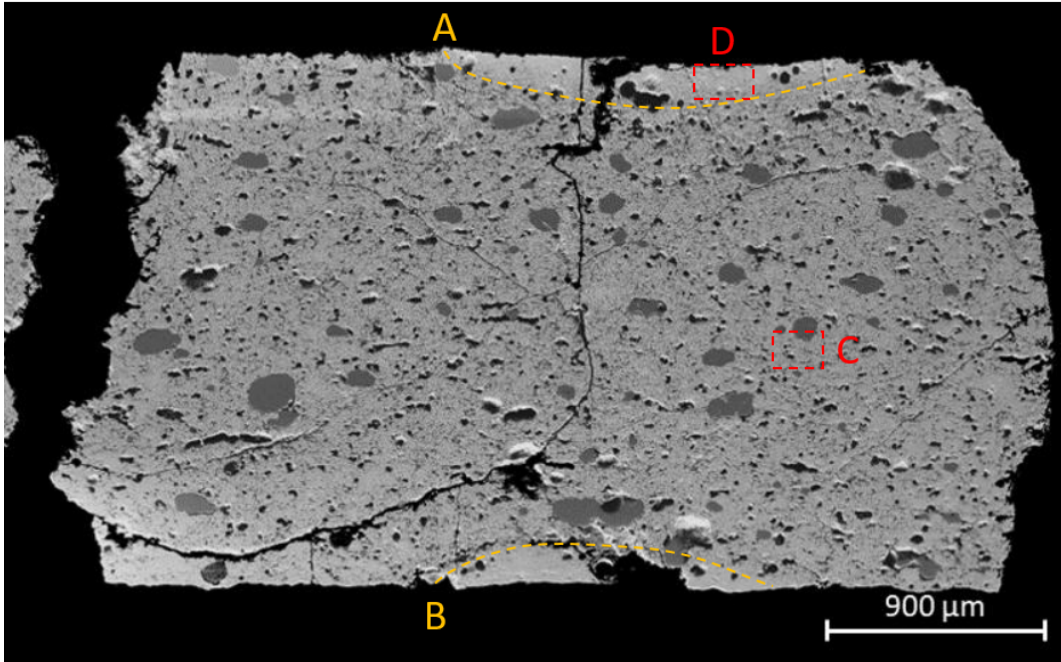


Figure 11: Cross-section of a MOX-corium sample.

- (iii) A  $\text{CaSiO}_X$  rich phase with a similar composition to that of as-sintered  $\text{UO}_2$ -corium is observed, with a  $\text{Si}/\text{Ca}$  ratio=1.28. XRD characterisation indicates, however, that the crystal structure is consistent with  $\text{Ca}_2\text{SiO}_4$ .
- (iv) A metallic phase rich in Fe (81.0 at.% Fe, in average) and Si (19.0 at.% Si, in average) is observed. The presence of metallic Si indicates that the oxygen chemical potential ( $\mu_{\text{O}_2}$ ) during sintering was lower than in  $\text{UO}_2$ -corium samples. XRD characterisations indicate this phase is consistent with  $\alpha$ -Fe.

#### Laser-melted region

A SEM-SE image acquired in the melted region of a MOX-corium sample is presented in Figure 14 (a), along with X-ray maps of elements Fe (b), Ca (c), Si (d), U (e), Pu (f) and Zr (g). This image and X-ray maps were acquired in region D, highlighted in Figure 11, but is rotated 180°, for consistency with  $\text{UO}_2$ -corium results: the periphery of the sample is located at the bottom of the image. The dashed line indicates the boundary between the melted and the re-sintered regions. As with  $\text{UO}_2$ -corium samples, the latter is a region in which the temperature was high enough to re-sinter the material, but not enough to melt it. Far from this boundary, towards the top of the image, the microstructure becomes similar to that of as-sintered material. Three main phases can be identified: (i) a single fluorite,  $(\text{U}, \text{Pu}, \text{Zr})\text{O}_{2\pm X}$ , (ii) a  $\text{Ca}, \text{Si}$ -rich oxide ( $\text{CaSiO}_X$ ), and (iii) a Fe-rich metallic phase ( $\alpha$ -Fe). The composition of these phases is presented in Figure 15. As observed, the size of the dendrites ( $\text{CaSiO}_X$  phase) is considerably lower than in  $\text{UO}_2$ -corium samples, so the surrounding phases likely interfered with the quantitative measurements.

The main observations are:

- (i) The microstructure of the melted region is similar to that of  $\text{UO}_2$ -corium samples: dendrites of Si- and

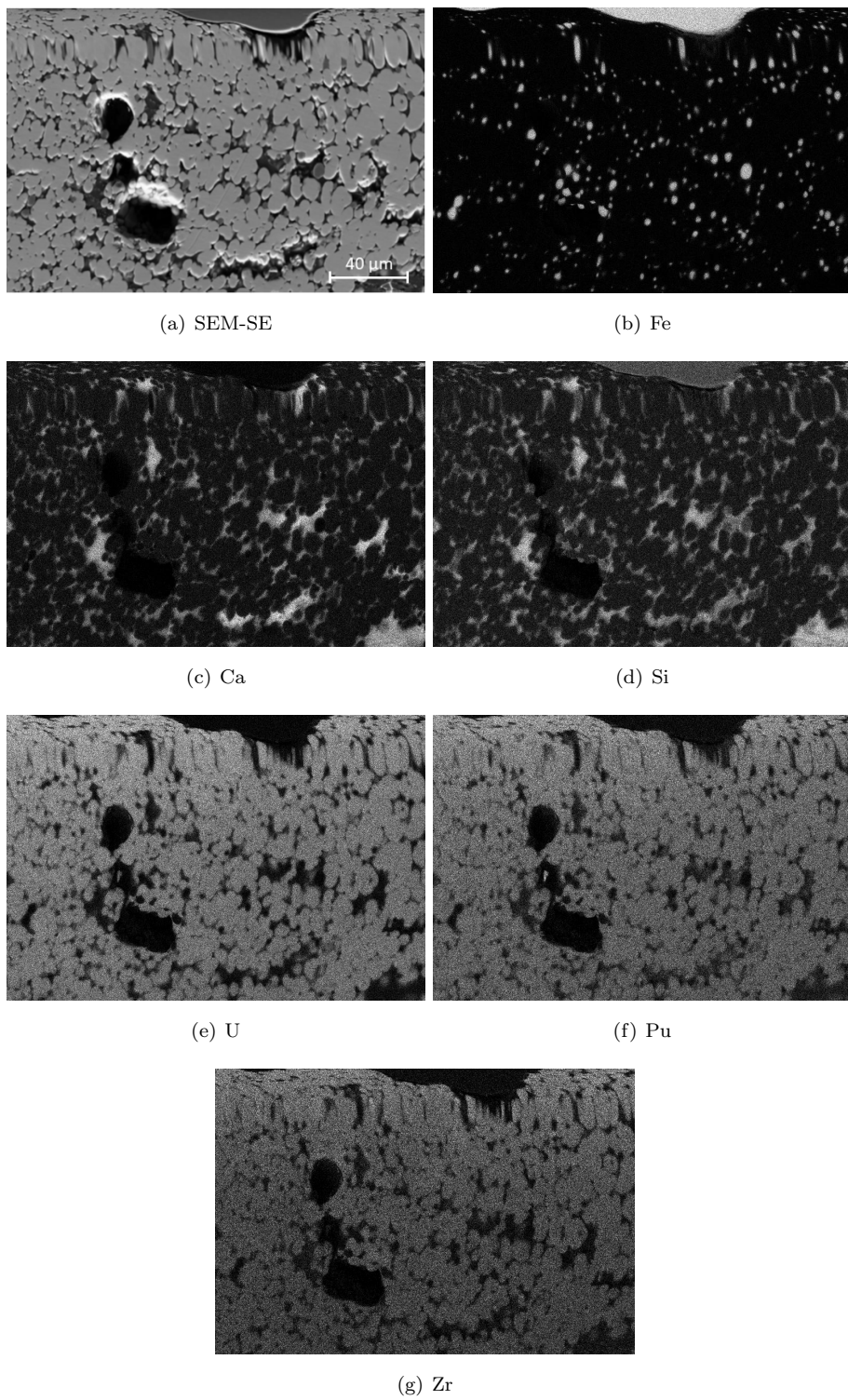
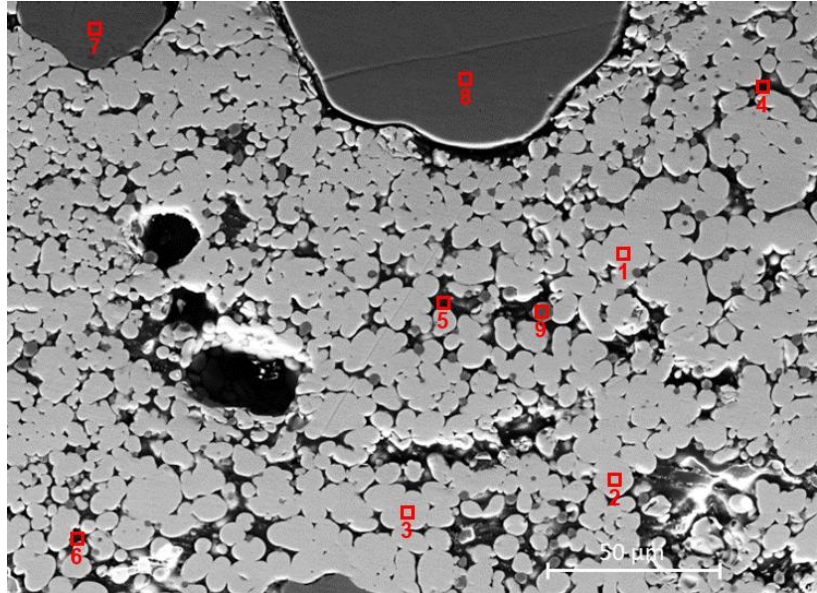


Figure 12: Fe, Ca, Si, U, Pu, and Zr X-ray maps acquired on a as-sintered MOX-corium sample.



Phase	Point	Composition (at.%)						
		O	Si	Ca	Fe	Zr	U	Pu
$(\text{U}, \text{Pu}, \text{Zr})\text{O}_2$	1	65.3	4.4	3.7	0.4	11.4	12.3	2.3
	2	65.2	3.8	3.9	0.4	10.9	13.3	2.4
	3	65.3	2.8	3.9	0.2	12.7	12.8	2.3
$\text{CaSiO}_X$	4	60.6	19.8	16.2	1.8	0.3	0.7	0.4
	5	61.6	20.7	15.1	0.2	0.6	1.2	0.6
	6	60.7	18.8	15.2	2.8	0.7	1.2	0.6
Metallic	7	0.0	19.5	0.0	80.5	0.0	0.0	0.0
	8	0.0	19.1	0.0	80.9	0.0	0.0	0.0
	9	0.0	18.4	0.0	81.6	0.0	0.0	0.0

Figure 13: Quantitative characterisation of an as-sintered MOX-corium sample.

Ca-rich oxide phase surrounding the fluorite phase,  $(\text{U}, \text{Pu}, \text{Zr})\text{O}_{2\pm X}$ . In MOX-corium, however, the fraction of dendrites is considerably lower than in the  $\text{UO}_2$  samples.

- (ii) The average O/M ratio of the fluorite in the melted region (points 2, 3, and 4 in Figure 15), is 1.81. These quantitative results, however, are likely affected by the composition of surrounding phases.
- (iii) The Si content in the  $\text{CaSiO}_X$  phase decreases towards the periphery of the melted region. The Si/Ca ratio measured in point 5 (far from the periphery) is 0.95, but in points 6 and 7 it is 0.54 and 0.67,

respectively. This suggest that Si was released during laser heating experiments.

- (iv) The Si content in the metallic precipitates decreases considerably towards the periphery of the sample: points 8 and 9 (both in the re-sintered region), 10.7 and 8.2 at.%Si, respectively, while in point 10 (the melted region), 2.3 at.% Si. This concentration gradient also suggests that Si was released during laser heating experiments.

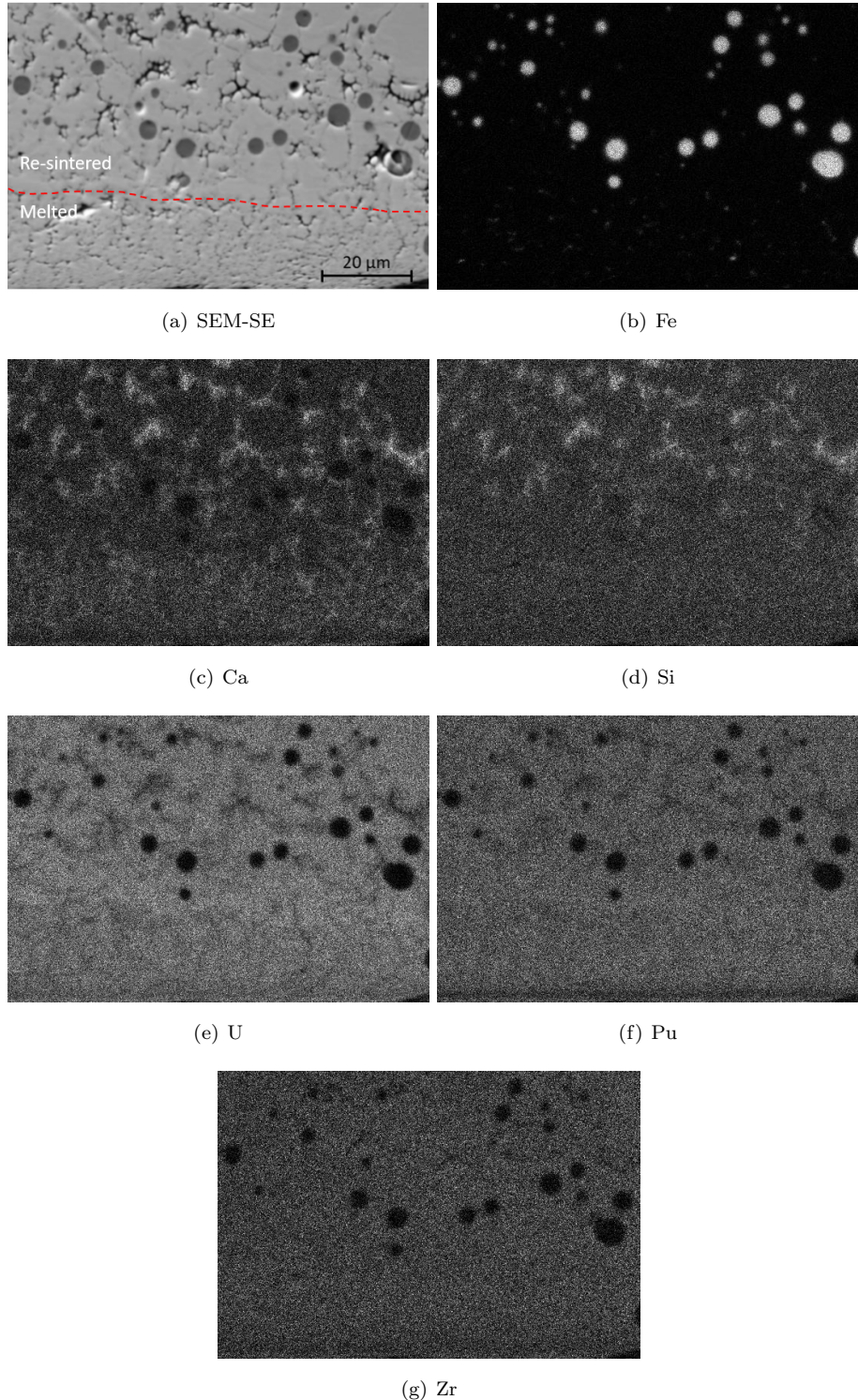
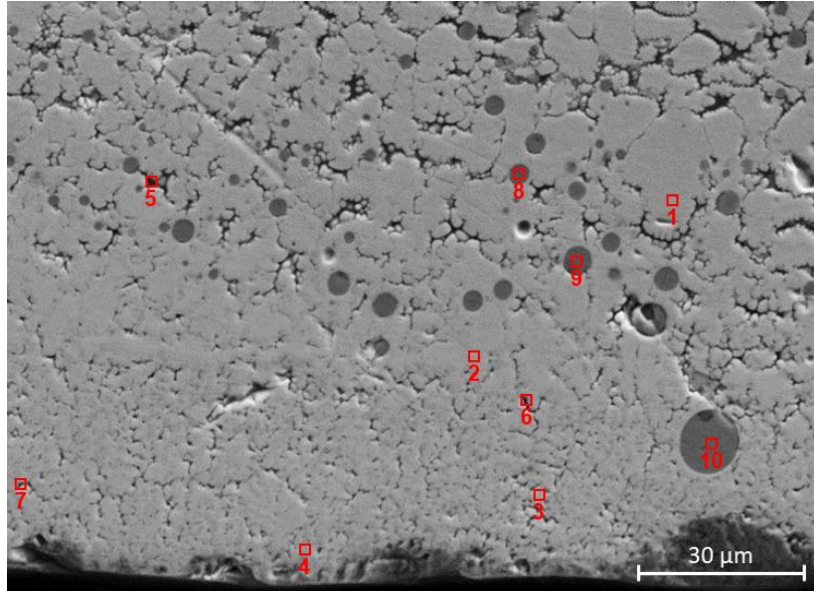


Figure 14: Fe, Ca, Si, U, Pu, and Zr X-ray maps acquired on the laser-melted region of a MOX-corium sample.



Phase	Point	Composition (at.%)						
		O	Si	Ca	Fe	Zr	U	Pu
(U, Pu, Zr)O <sub>2</sub>	1	65.1	4.4	4.2	0.4	11.5	12.2	2.1
	2	65.3	3.8	3.8	0.4	10.3	14.1	2.3
	3	64.1	5.5	7.0	0.6	8.6	11.7	2.3
	4	64.0	5.0	7.1	0.7	9.6	11.2	2.2
CaSiO <sub>X</sub>	5	61.1	15.5	16.2	0.5	2.7	2.9	1.1
	6	61.7	8.0	14.7	0.2	6.6	7.1	1.6
	7	61.6	8.0	12.0	3.3	6.6	6.9	1.5
$\alpha$ -Fe	8	0.2	10.7	0.0	89.1	0.0	0.1	0.0
	9	0.1	8.2	0.1	91.6	0.0	0.0	0.0
	10	0.0	2.3	0.0	97.7	0.0	0.0	0.0

Figure 15: Quantitative characterisation of the laser-melted region on a MOX-corium sample.

### 3.1.3. X-Ray Diffraction

XRD characterisation was conducted on as-sintered UO<sub>2</sub>- and MOX-corium samples. The recovery of melted material from both systems was also attempted, but it was not possible to fully isolate it from as-sintered material. As a consequence, the obtained results on melted and as-sintered material were either similar or highly overlapped, preventing a more detailed analysis of the systems' evolution. Therefore, only the results acquired on as-sintered samples are presented here.

## **UO<sub>2</sub>-corium**

The diffractogram collected on as-sintered UO<sub>2</sub>-corium is presented in Figure 16, along with those of the refined reference materials. The crystal structures identified through XRD are: two fluorite phases ((U, Zr)O<sub>2±X</sub>#1 and #2), a wollastonite phase (CaSiO<sub>3</sub>, monoclinic structure), and a BCC phase ( $\alpha$ -Fe). The diffractograms in Figure 16 have been shifted vertically for ease of comparison. The highlighted regions offer detail of the contribution of selected reference structures to the diffractogram of the whole sample. The refined lattice parameters of these structures and those of pure reference materials are presented in Table 5. A difference can be observed in the relative intensity of the diffraction lines of a same structure in the experimental diffractogram. This can be attributed to a preferred orientation of crystals, likely due to the reduced amount of sample used for the characterisations and to the fact the sample was not spinning during XRD characterisation. It was not possible therefore to determine the phase fraction of the identified phases on the sample diffractogram. Observations are summarized as follows:

- (i) The lattice parameters of both fluorite phases are smaller than that of the reference. This is consistent with the observations of Zheng, et al., where a decrease of the fluorite lattice parameter was observed with increased fractions of ZrO<sub>2</sub> [11].
- (ii) The BCC phase is consistent with  $\alpha$ -Fe. The refined lattice parameter of this structure is smaller than that of the reference. This could be due to an effect of temperature or to the small presence of Si. Indeed, it is reported in literature that the lattice parameter of a BBC solution with 9 at.%Si in Fe is 2.843 Å[12].
- (iii) A wollastonite structure (low temperature allotrope of CaSiO<sub>3</sub>) was also identified in the UO<sub>2</sub>-corium sample. Figure 16 shows in detail the contribution of this structure to the sample diffractogram.

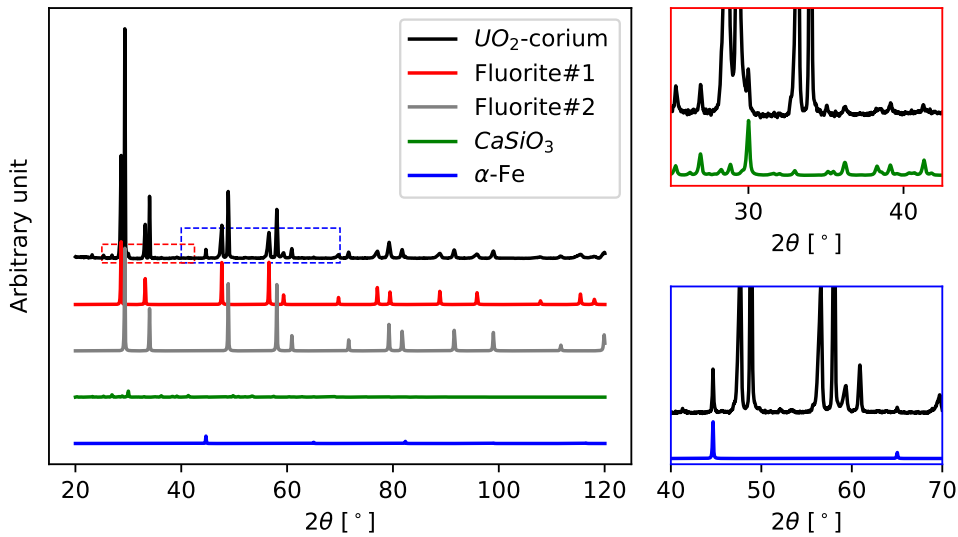


Figure 16: Diffractogram collected on as-sintered UO<sub>2</sub>-corium and identified phases.

Table 5: Refined lattice parameters of the phases identified in as-sintered UO<sub>2</sub>-corium samples by XRD.

Phase	Lattice Parameter (Å)		
		Refined	Reference
(U, Zr)O <sub>2±X</sub> #1 (Fluorite)	a	5.390	5.473
(U, Zr)O <sub>2±X</sub> #2 (Fluorite)	a	5.264	5.473
α - Fe (BCC)	a	2.866	2.874
	a	15.405	15.360
CaSiO <sub>3</sub> (Wollastonite)	b	7.319	7.285
	c	7.057	7.084
	β	95.089	95.4

### MOX-corium

The diffractogram collected on as-sintered MOX-corium is presented in Figure 17, along with those of the refined reference materials. The crystal structures identified through XRD are: a fluorite phase ((U, Zr)O<sub>2±X</sub>), an olivine phase (Ca<sub>2</sub>SiO<sub>4</sub>, monoclinic structure), and a BCC phase (α-Fe). The diffractograms in Figure 16 have been shifted vertically for ease of comparison. The highlighted regions offer detail of the contribution of selected reference structures to the diffractogram of the whole sample. The refined lattice parameters of these structures and those of pure reference materials are presented in Table 5. Similarly to results acquired on the UO<sub>2</sub>-corium sample, the relative intensity of the diffraction lines does not match that of the reference structures. Again, this can be attributed to a preferred orientation of crystals caused by the small quantity of sample or to the sample holder being stationary during data acquisition. As a consequence, it was not possible to determine the phase fraction of the identified phases on the sample diffractogram. Observations are summarized below.

- (i) A single fluorite phase is observed, with a refined lattice parameter of 5.315 Å. This lattice parameter is in-between those of the two fluorite phases observed in UO<sub>2</sub>-corium samples in 5, which makes sense given the measured compositions and Vegard's Law.
- (ii) A diffraction pattern in this sample is consistent with an olivine (monoclinic) structure. The latter is a Ca<sub>2</sub>SiO<sub>4</sub> phase, in which Fe cations can substitute Ca ones. However, the Si/Ca ratio determined experimentally is not consistent with this structure. A possible reason for this inconsistency is that experimental conditions (e.g., low  $\mu$ O<sub>2</sub>) or the incorporation of other elements (e.g., Pu) could have stabilized the olivine structure.
- (iii) Experimental data would also suggest that there is a pseudo-wollastonite structure (monoclinic), al-

though it is not conclusive and therefore not included in the results. This structure is the high temperature ( $> 1398$  K) allotrope of the wollastonite structure ([13]) and it is unlikely to be present in the sample. As with the olivine structure, the incorporation of certain elements could have stabilized the pseudo-wollastonite structure at lower temperatures.

- (iv) The refined lattice parameter of the  $\alpha$ -Fe phase (BCC) is  $2.843$  Å, lower than that of the same phase in the  $UO_2$ -corium sample. This is in good agreement with literature, as it has been reported that an increased Si content would reduce the lattice parameter of the BCC phase [12].

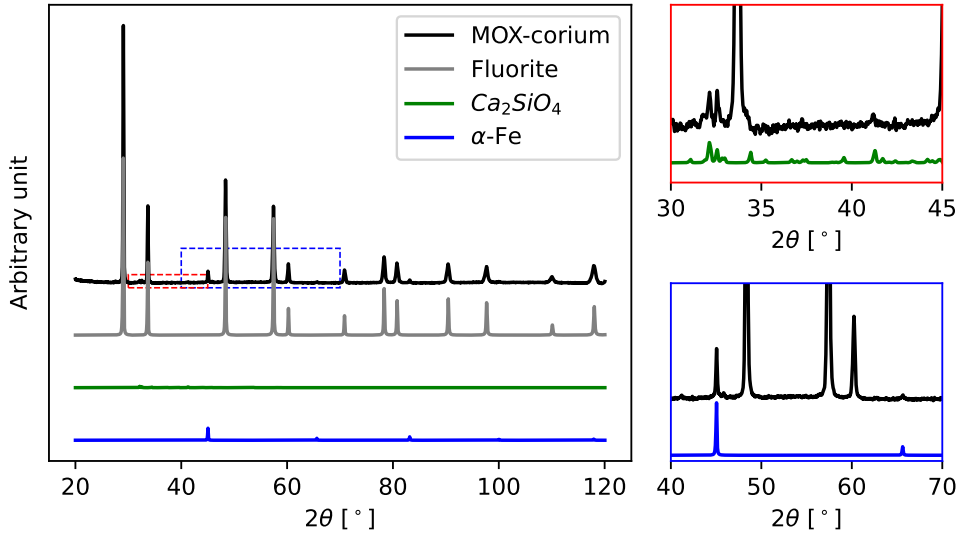


Figure 17: XRD characterisation on a as-sintered MOX-corium sample.

### 3.1.4. Knudsen Effusion Mass Spectrometry (KEMS)

KEMS characterisation was conducted only on an as-sintered MOX-corium sample, with the focus on the vapour pressure of  $UO_x$ ,  $PuO_x$ , and  $ZrO_x$  species. Due to the interference and overlapping of many isotopes of Si and Ca with background noise caused by  $N_2$ ,  $CO_2$ , and hydrocarbons, the vapour pressure of these light species could not be quantified. Experimental results are presented in Figure 18, along with two sets of thermodynamic calculations: The vapour pressure of species calculated with the TAF-ID (v.15) considering the composition of the MOX-corium samples (left, solid lines), and considering pure stoichiometric  $MO_2$  compounds (with  $M = U$ ,  $Pu$ ,  $Zr$ ; right, dashed lines). Regarding calculations considering the nominal composition of the MOX-corium system, the oxygen stoichiometry was estimated from the Si content in metallic phases: the oxygen content of the system was calculated with the TAF-ID, as that which would produce the fraction of Si in metallic state that was observed experimentally by SEM-EDS.

The vapour pressure of species calculated with an oxygen content estimated from SEM-EDS results is in very good agreement to KEMS observations, especially when comparing experimental results to those calculated for pure stoichiometric compounds. This highlights the sensitivity of the system to the oxygen content. The difference between calculations and experimental results can be attributed to a combination

Table 6: Refined lattice parameters of the phases identified in as-sintered MOX-corium by XRD.

Phase	Lattice Parameter (Å)		
		Refined	Reference
(U, Pu, Zr) $O_{2\pm x}$ (Fluorite)	a	5.315	5.473
$\alpha - Fe$ (BCC)	a	2.843	2.874
$Ca_2SiO_4$ (Olivine)	a	5.508	5.510
	b	6.741	6.760
	c	9.310	9.320
	$\beta$	94.5	94.5

of several factors: (1) the inherent uncertainty in the experimental determination of the composition of phases (Si and Fe, in this case) by SEM-EDS; (2) uncertainties related to the determination of vapour pressures using KEMS, including mainly temperature error, appearance potential correction, and cross-section determination; (3) inaccuracies in thermodynamic models, either Si-Fe-O (since the oxygen content is estimated from the Si/Fe ratio in equilibrium with the oxygen partial pressure) or binaries/ternaries systems in U-Pu-Zr-O; (4) the evolution of the oxygen content of the sample during KEMS as species are released; and (5) the composition of sample used in the KEMS experiment might have not been fully representative of the global pellet composition (ratio between phases not representative of the full pellet, leading to differences in oxygen content of the KEMS sample).

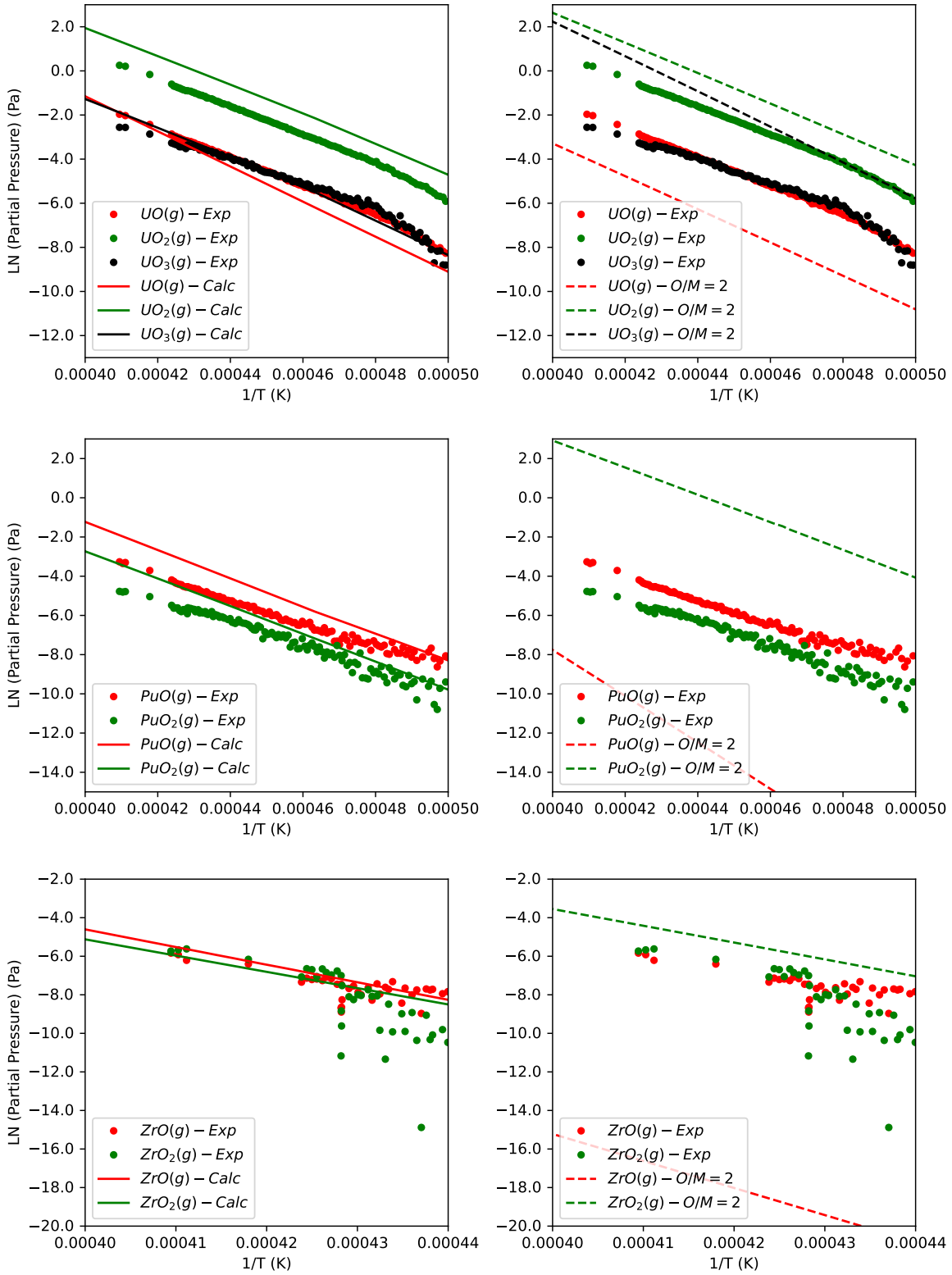


Figure 18: Vapour pressure of  $\text{UO}_X$ ,  $\text{PuO}_X$ , and  $\text{ZrO}_X$  species in MOX-corium determined by KEMS. Results are compared to thermodynamic calculations considering the oxygen content estimated by SEM-EDS (left) and to pure stoichiometric phases ( $\text{O}/\text{M}=2$ ):  $\text{UO}_2$ ,  $\text{PuO}_2$ , and  $\text{ZrO}_2$  (right).

### 3.2. Thermodynamic Calculations

The phases in equilibrium in  $\text{UO}_2$ - and MOX-corium samples have been calculated with Thermocalc and the TAF-ID v.15, from the maximum temperature measured in laser experiments (3200 K) to 1500 K. At the latter temperature, all the phases in both systems are predicted to be solid and can be considered not to evolve any further due to kinetic constraints (besides structural allotropes). One of the main inputs for these calculations is the oxygen content of the systems, as it has a major impact on the chemical state of all elements. The nominal oxygen content (from the pure compounds used for preparing the samples) cannot be used due to the impact of the reducing atmosphere during the sintering process. Therefore, the oxygen content in the samples has been estimated from SEM-EDS results, particularly the composition of the metallic phases. Indeed, several equilibrium calculations at the sintering temperature (*i.e.*, 1873 K) have indicated that Si acts as buffer, oxidizing to  $\text{SiO}_2$  with increasing  $\text{O}_2$  contents, while the other phases remain relatively unchanged. Therefore, the oxygen content considered for each system is that which results in the Si fraction observed in the metallic phases in as-sintered samples (same approach as for of KEMS calculations). The composition of each system considered for calculations is presented in Table 7. Calculations on the  $\text{UO}_2$ -corium system are presented first and compared to experimental results, followed by those on the MOX-corium system.

Table 7: System composition for thermodynamic calculations. The oxygen content is estimated from the composition of metallic phases in as-sintered samples.

System	Composition (at.%)						
	O	Si	Ca	Fe	Zr	U	Pu
$\text{UO}_2$ -Corium	59.38	6.52	6.99	7.95	9.37	9.79	-
MOX-Corium	57.67	6.62	7.10	8.07	9.51	9.94	1.08

#### 3.2.1. $\text{UO}_2$ corium system

The calculated evolution of the system composition (phase mass fraction) between 3200 and 1500 K for the  $\text{UO}_2$ -corium system is presented in Figure 19. The following phases are calculated in this temperature range: a gas phase, three liquid phases (Liquid#1, Liquid#2, and Liquid#3), two fluorite phases (Fluorite#1 and Fluorite#2, along with the calculated O/M ratio of each), and one BCC, FCC, Pseudo-Wollastonite, and Tetragonal-ZrO<sub>2</sub> phase. The composition vs. temperature of the gas phase is presented in Figure 20, and that of all the relevant condensed phases in Figure 21.

TAF-ID calculations indicate that:

- Between 3200 and 3029 K, only two phases exist in equilibrium: A gas phase, consisting mainly of  $\text{Fe}_{(g)}$  and  $\text{SiO}_{(g)}$ , and an oxide liquid phase (Liquid#1), which contains every element in the system that is not in the gaseous state.
- Between 3029 and 2923 K, the gas phase condenses into a metallic liquid (Liquid#2), which consists mainly of Fe with up to 2.5 at.% Si and 1.5 at.% O.

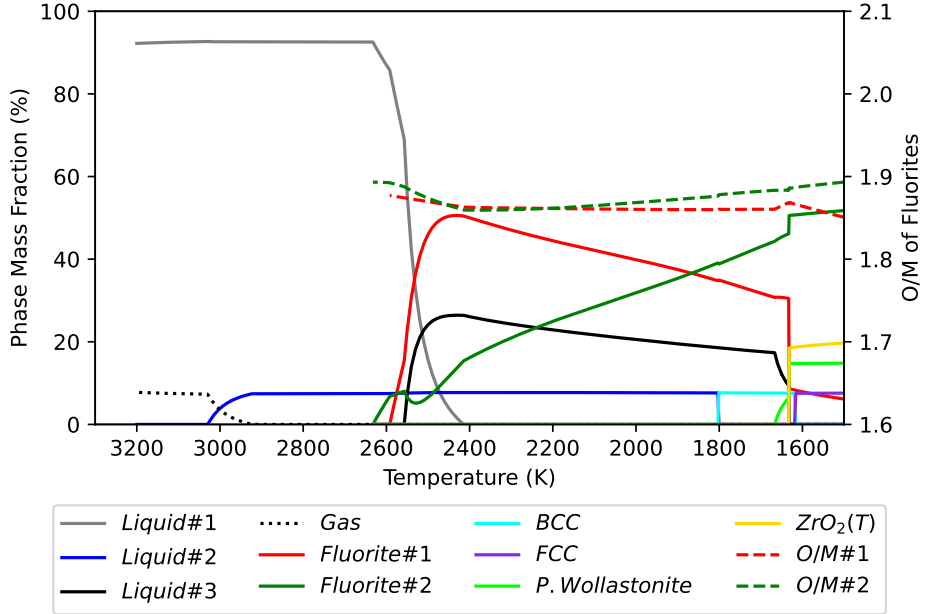


Figure 19: Phases in equilibrium calculated in UO<sub>2</sub>-corium samples, as temperature decreases from the maximum laser temperature, 3200 K.

- Between 2632 and 2414 K, Liquid#1 solidifies and two fluorite phases are created: Fluorite#1, which starts with an even ratio of U and Zr but becomes richer in Zr as temperature decreases, and Fluorite#2, which is rich in U at all temperatures and contains only traces of Zr. Fluorite#1 contains up to 5.1 at.% Ca and Fluorite#2 up to 5.2 at.% Fe. According to calculations, both fluorite phases are highly hypo-stoichiometric, with an average O/M=1.88.
- A third liquid phase (Liquid#3) is segregated from Liquid#1 as it solidifies. This liquid consists mainly of Ca, Si, and O, but it can dissolve important quantities of U at high temperature (up to 7.7 at.% U at 2632 K).
- Between 2414 and 1670 K, the number of phases in the system remains constant. The metallic Liquid#2 solidifies into a BCC phase with the same composition (mostly Fe) around 1800 K. The phase fraction of the U-rich Fluorite#2 increases as temperature decreases, incorporating U formerly present in the Si-Ca-O rich Liquid#3 phase and the Zr-rich Fluorite#1 phase.
- At 1670 K, the Si-Ca-O rich Liquid#3 phase solidifies into a pseudo-wollastonite structure (CaSiO<sub>3</sub>). Lastly, Tetragonal-ZrO<sub>2</sub> is formed from the Zr-rich Fluorite#1 phase at 1632 K.

### 3.2.2. Comparison of Experimental and Calculation Results

#### As-sintered UO<sub>2</sub>-corium

The phases observed experimentally and those calculated with the TAF-ID at the sintering temperature are summarized in Table 8. Four phases were identified in as-sintered UO<sub>2</sub>-corium by SEM-EDS and XRD: (i) A first (U,Zr)O<sub>2</sub> fluorite phase, richer in Zr (11.2 at.% Zr and 9.8 at.% U, on average), (ii) a second

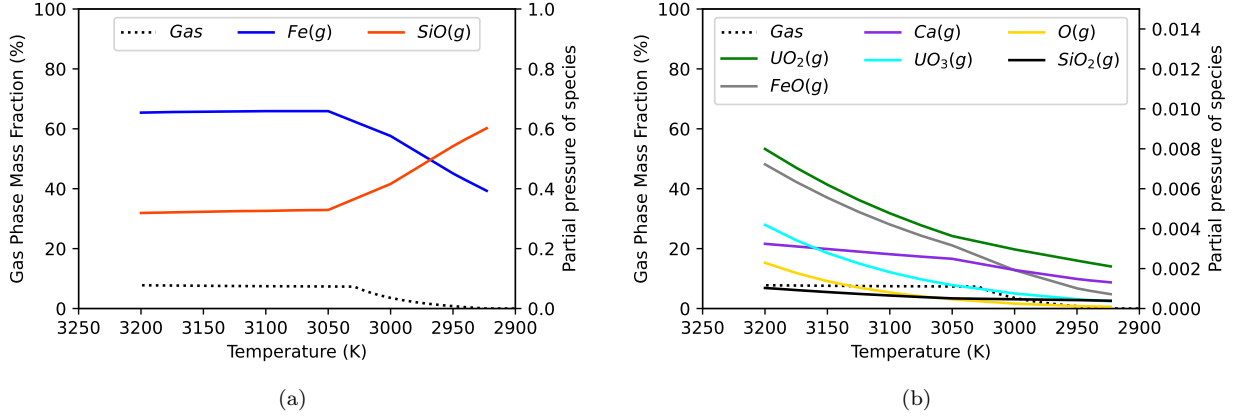


Figure 20: Calculated vapour pressure of main (a) and minor (b) species in the gas phase,  $\text{UO}_2$ -corium system.

$(\text{U}, \text{Zr})\text{O}_2$  fluorite with a lower Zr content (2.4 at.% Zr and 10.8 at.% U, on average), a wollastonite phase ( $\text{SiCaO}_3$ ), and a metallic Fe phase with BCC structure, consistent with  $\alpha$ -Fe (99.3 at.% Fe, 0.6 at.% Si). At 1873 K (sintering temperature), the following phases are calculated by the TAF-ID: (i) A first  $(\text{U}, \text{Zr})\text{O}_2$  fluorite phase (Fluorite#1), richer in Zr (23.8 at.% Zr and 6.2 at.% U), (ii) a second  $(\text{U}, \text{Zr})\text{O}_2$  fluorite phase (Fluorite#2), richer in U (4.6 at.% Zr and 29.8 at.% U), a Si-Ca-O rich liquid with a composition consistent with  $\text{SiCaO}_3$ , and a Fe-rich metallic Liquid#2. The calculated composition of the latter liquid is in excellent agreement with observations, as it was this composition one of the condition for calculations. The calculated Liquid#3 phase is also in excellent agreement with the wollastonite phase ( $\text{SiCaO}_3$ ) observed experimentally. Although a miscibility gap in the fluorite phase is calculated by the TAF-ID, with one fluorite being richer in Zr and the other richer in U, there is a considerable difference in the calculated and measured composition. This difference would then imply that the U-Zr-O model in the TAF-ID should be revised, but the possibility of the experimental system being not in chemical equilibrium and the inherent uncertainties of the experimental techniques must be considered.

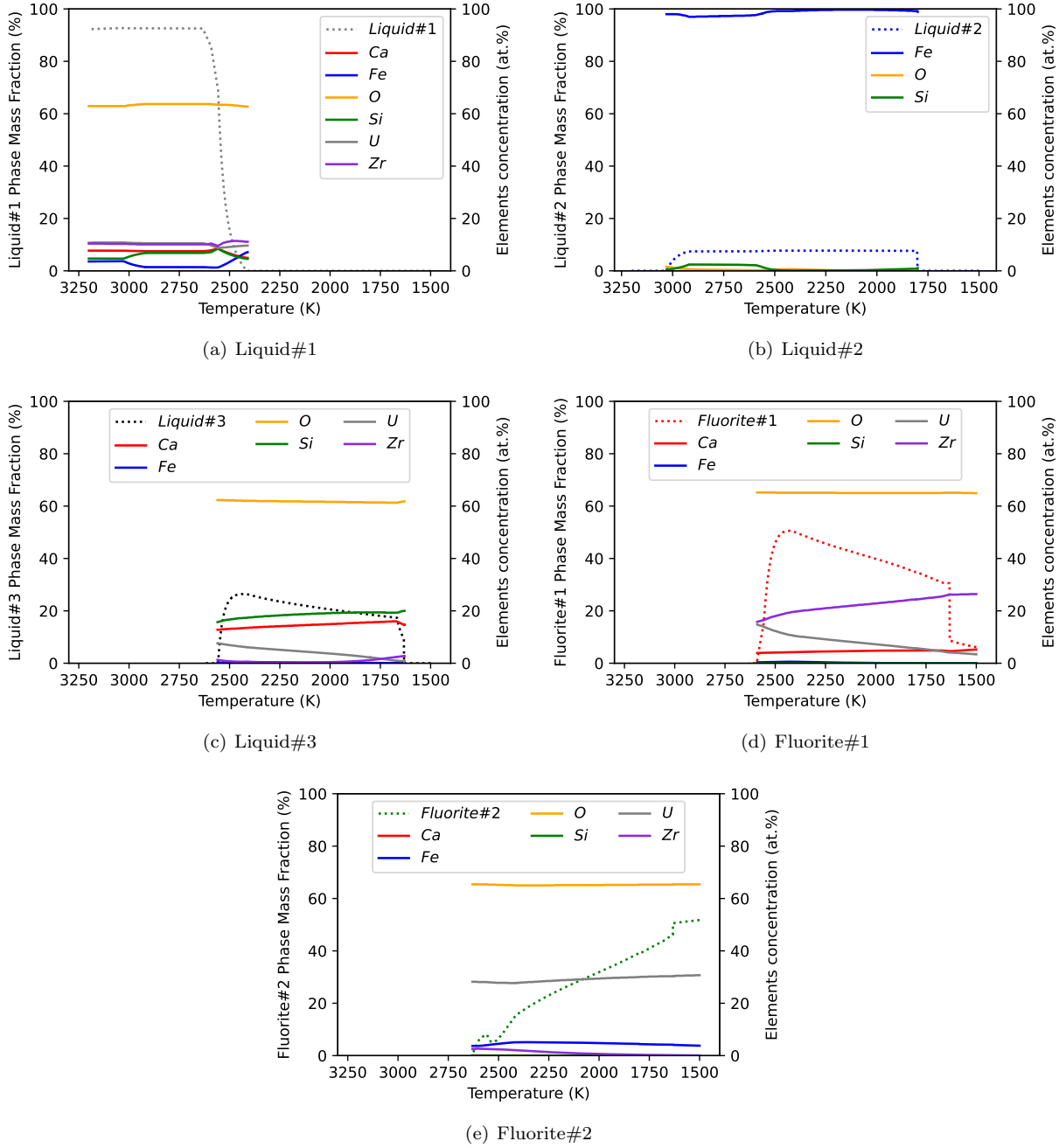


Figure 21: Calculated evolution with temperature of the composition of main phases in a  $\text{UO}_2$ -corium system.

Table 8: Comparison of the experimentally measured and calculated composition at 1873 K of phases in as-sintered UO<sub>2</sub>-corium.

	Phase	Composition (at.%)					
		O	Si	Ca	Fe	Zr	U
SEM-EDS	Fluorite#1	65.0 ± 0.1	9.1 ± 0.3	4.2 ± 0.2	0.6 ± 0.2	11.3 ± 0.7	9.8 ± 0.1
	Fluorite#2	63.7 ± 0.1	14.2 ± 0.1	8.5 ± 0.2	0.5 ± 0.0	2.4 ± 0.2	10.8 ± 0.3
	α-Fe	0.1 ± 0.0	0.6 ± 0.0	0.0 ± 0.0	99.2 ± 0.0	0.0 ± 0.0	0.0 ± 0.0
	CaSiO <sub>X</sub>	60.9 ± 0.1	19.5 ± 0.8	15.6 ± 1.2	1.7 ± 1.0	1.3 ± 0.4	1.1 ± 0.6
TAF-ID	Fluorite#1	65.0	0.0	4.9	0.0	23.8	6.2
	Fluorite#2	65.2	0.0	0.0	4.6	0.4	29.8
	Liquid#2	0.0	0.6	0.0	99.4	0.0	0.0
	Liquid#3	61.5	19.4	15.4	0.1	0.8	2.8

#### Laser Heating on UO<sub>2</sub>-corium

Laser heating experiments determined the solidus and liquidus temperatures of the material. Calculations and experiments do indicate, however, that there is not a single liquid in the system at high temperature (there are, at least, an oxide and a metallic liquids predicted in the system). Then, the experimental liquidus and solidus temperatures would correspond to those of the Liquid#1 phase calculated by the TAF-ID (containing every element other than those in metallic state), which constitutes most of the sample. Experimental and calculated values are compared in Table 9, being the experimental uncertainty the sum of the average deviation of obtained results and systematic experimental errors. As observed, there is a great agreement between experimental and calculated values and the small differences are within experimental errors. No evidence was observed experimentally of a miscibility gap in the fluorite phase in the melted region, although it is calculated by the TAF-ID and it was observed in the as-sintered material. This difference can be attributed either to the models that would not describe accurately the behaviour of the system (meaning that the miscibility gap should appear at lower a temperature, similarly to calculations of the MOX-corium system) or simply to a consequence of the extremely fast cooling rate. The impact of the latter on such a complex system is not well understood and no conclusions can be drawn. The Fe concentration gradient in the CaSiO<sub>X</sub> phase observed on the X-ray maps acquired on the melted region (Figure 9) was attributed to the oxidation during the laser experiments. TAF-ID calculations support this hypothesis, as can be observed in Figure 22. The latter correspond to the evolution of the mass fraction of the metallic Liquid#2 and the (Si,Ca,O)-rich Liquid#3 with varying oxygen chemical potential ( $\mu O_2$ ) at 2400 K, along with the evolution of the Liquid#3 composition. According to calculations, as the  $\mu O_2$  increases the metallic liquid phase eventually disappears due to Fe oxidation, which joins the (Si,Ca,O)-rich liquid. Above -314 kJ/Kmol<sub>O2</sub> Fe would be completely oxidized, reaching a maximum concentration of 13.1 at.% Fe in the (Si,Ca,O)-rich liquid. This is in excellent agreement with experimental observations (refer to Figure 10).

Table 9: Experimental and calculated Liquidus and Solidus temperatures of the  $\text{UO}_2$ -corium system.

	Experimental (K)	Calculated (K)
Liquidus	$2633 \pm 38$	2632
Solidus	$2443 \pm 25$	2414

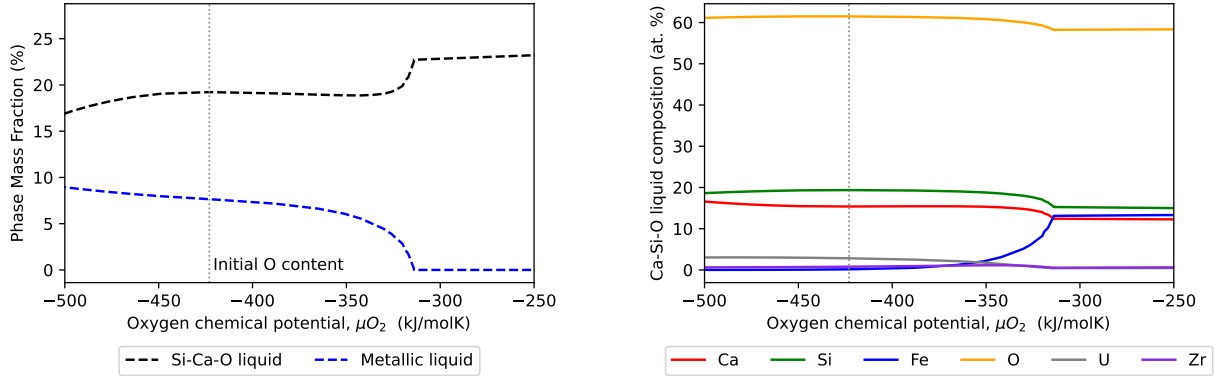


Figure 22: Evolution of the metallic and Si-Ca-O liquid phases and their composition at 2400 K and varying oxygen chemical potential ( $\mu\text{O}_2$ ) in the  $\text{UO}_2$ -corium system. The vertical line indicates the initial oxygen content of the system, estimated by SEM-EDS. As the  $\mu\text{O}_2$  increases during laser experiments due to oxygen capture, Fe tend to oxidize and join the Ca-Si-O liquid.

### 3.2.3. MOX-corium system

The calculated evolution of the MOX-corium system composition with temperature is presented in Figure 23. As for the  $\text{UO}_2$ -corium system, the temperature range considered for calculations is between 3200 K (maximum temperature in laser heating experiments) and 1500 K (temperature at which all the calculated phases are predicted to be solid and can be considered not to evolve any further). In this temperature range, the main calculated phases are: a gas phase, two liquid phases (Liquid#1 and Liquid#2), two fluorite phases (Fluorite#1 and Fluorite#2), a BCC phase, a pseudo-Wollastonite phase, and a tetragonal-ZrO<sub>2</sub> phase. The evolution of the gas phase composition is presented in Figure 24, and that of the relevant condensed phases in Figure 25.

TAF-ID calculations on this system are summarized as follows:

- Between 3200 and 3009 K, two phases are in equilibrium: a gas phase that consists mainly of  $\text{Fe}_{(g)}$  and  $\text{SiO}_{(g)}$  and represents 12 wt.% of the system at 3200 K; and an oxide liquid phase (Liquid#1), which contains every element in the system that is not in the gaseous state.
- Between 3009 and 2758 K, the gas phase condenses into a metallic liquid (Liquid#2). The latter consists mainly of Fe and Si (82 and 17 at.%, respectively, at 2758 K).
- Liquid#1 starts solidifying at 2947 K into a single fluorite phase (Fluorite#1). As the fluorite phase forms upon cooling, Liquid#1 becomes rich in concrete elements (*i.e.*, Si, Ca, and O). This behaviour is different

to that calculated for the UO<sub>2</sub>-corium system where the Si-Ca-O rich liquid segregated from the initial Liquid#1 into a separate phase. The sharp decrease of the Liquid#1 mass phase fraction continues down to 2590 K.

- Below 2590 K, U joins progressively the Fluorite#1 phase from the liquid until 2174 K, where a U-rich Fluorite#2 is created due to a miscibility gap (Figure 25 (a)). As temperature decreases, the Fluorite#1 becomes richer in Zr.
- Both fluorite phases are hypo-stoichiometric in the considered temperature range with an  $O/M < 1.9$ . Furthermore, calculations indicate that Ca and Pu have a higher affinity for the Zr-rich Fluorite#1 phase, while Fe has a higher affinity for the U-rich Fluorite#2 phase.
- The remainder of Liquid#1 solidifies at 1687 K mainly into CaSiO<sub>3</sub> (pseudo-wollastonite), and the metallic Liquid#2 into a BCC (Fe-Si intermetallic) at 1608 K.

As mentioned, the phase fraction of Liquid#1 decreases sharply with temperature as it solidifies and the Fluorite#1 phase is created. The latter occurs between 2947 and 2590 K, which can be considered as the liquidus and solidus temperatures, respectively. This is of course not strictly correct from a thermodynamic point of view, as the solidus temperature is the lowest temperature at which a liquid is present in the system, but rather a simplification in order to compare calculations to laser heating experimental results.

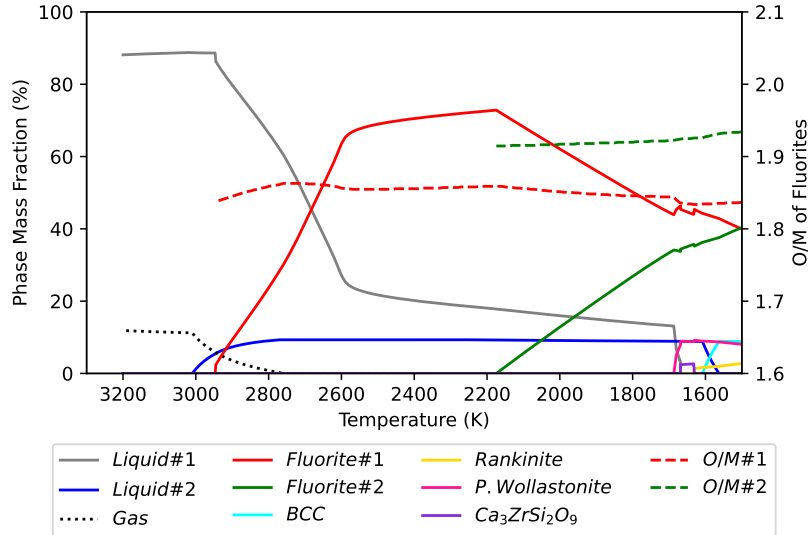


Figure 23: Phases in equilibrium calculated in a MOX-corium system as temperature decreases from the maximum laser temperature, 3200 K.

### 3.3. Comparison of Experimental and Calculation Results

#### As-sintered MOX-corium

Experimental observations and calculation results on as-sintered MOX-corium are summarized in Table 10. As a reminder, the oxygen content that was considered for calculations is that which results in the

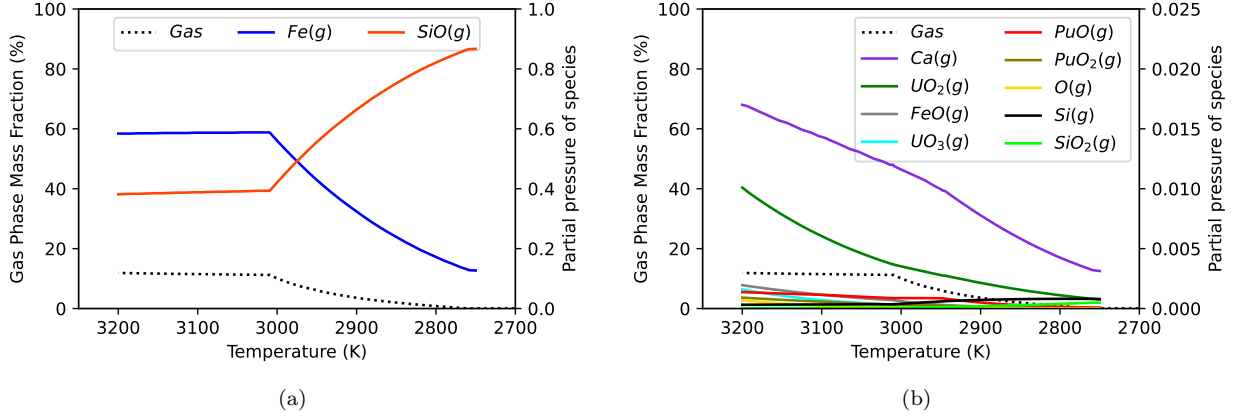


Figure 24: Calculated partial pressure of main (a) and minor (b) species in the gas phase, MOX-corium system.

composition observed experimentally for the metallic phase (*i.e.*, 19.0 at.%Si). This phase and its composition are therefore accurately reproduced by calculations, although at the sintering conditions it is in a liquid state (Liquid#1). The TAF-ID predicts three other phases at 1873 K: an oxide liquid phase, which mainly contains Si, Ca, and O (Liquid#2), and two fluorite phases (#1, rich in Zr, and #2, rich in U). The Si-Ca-O liquid is consistent with the  $CaSiO_x$  phase observed experimentally. Although there is a difference between the calculated and measured compositions of the latter phase, it is too small to consider a practical disagreement. This difference can be attributed to a contribution from surrounding phases or to the sample not being in thermodynamic equilibrium (diffusion and dissolution of U, Pu, and Zr, for instance).

There is a disagreement, however, regarding the miscibility gap in the fluorite phase. Only one fluorite phase is observed experimentally (confirmed by XRD and SEM-EDS), while two fluorite phases are calculated by the TAF-ID. According to calculations presented in Figure 23, the miscibility gap occurs below 2174 K. Therefore, there is a difference of 301 K between the calculated and observed temperature of immiscibility. Three potential reasons may have caused this difference: (i) the thermodynamic model of the U-Zr-O system in the TAF-ID system is inaccurate and it fails to predict the temperature at which the miscibility gap appears; (ii) the Fe-Si-O thermodynamic model is inaccurate, implying that the estimated oxygen content in the sample is incorrect (as the Si ratio in the metallic phase has been considered to calculate the  $\mu_{O_2}$  of the system); and (iii) the sample was not in chemical equilibrium and the oxygen chemical potentials of the phases are not related. The latter potential cause is highly unlikely since no concentration gradients (which would imply a state of non-equilibrium) were observed in either sample. Then, the disagreement in the temperature at which the miscibility gap appears must be related to the thermodynamic models of the mentioned systems or the experimental determination of the oxygen content. The impact of the latter on the miscibility gap temperature is explored in Figure 26: calculations indicate that an increasing Si content in the metallic phase (and consequent reduction of the oxygen chemical potential of the system) decreases the temperature at which the miscibility gap appears, from 2174 K (19.0 at.% Si in metallic phase) to 2049 K (dashed lines, corresponding to 25.0 at.% Si) and 1929 K (dotted lines, corresponding to 30.0 at.% Si in metallic phase).

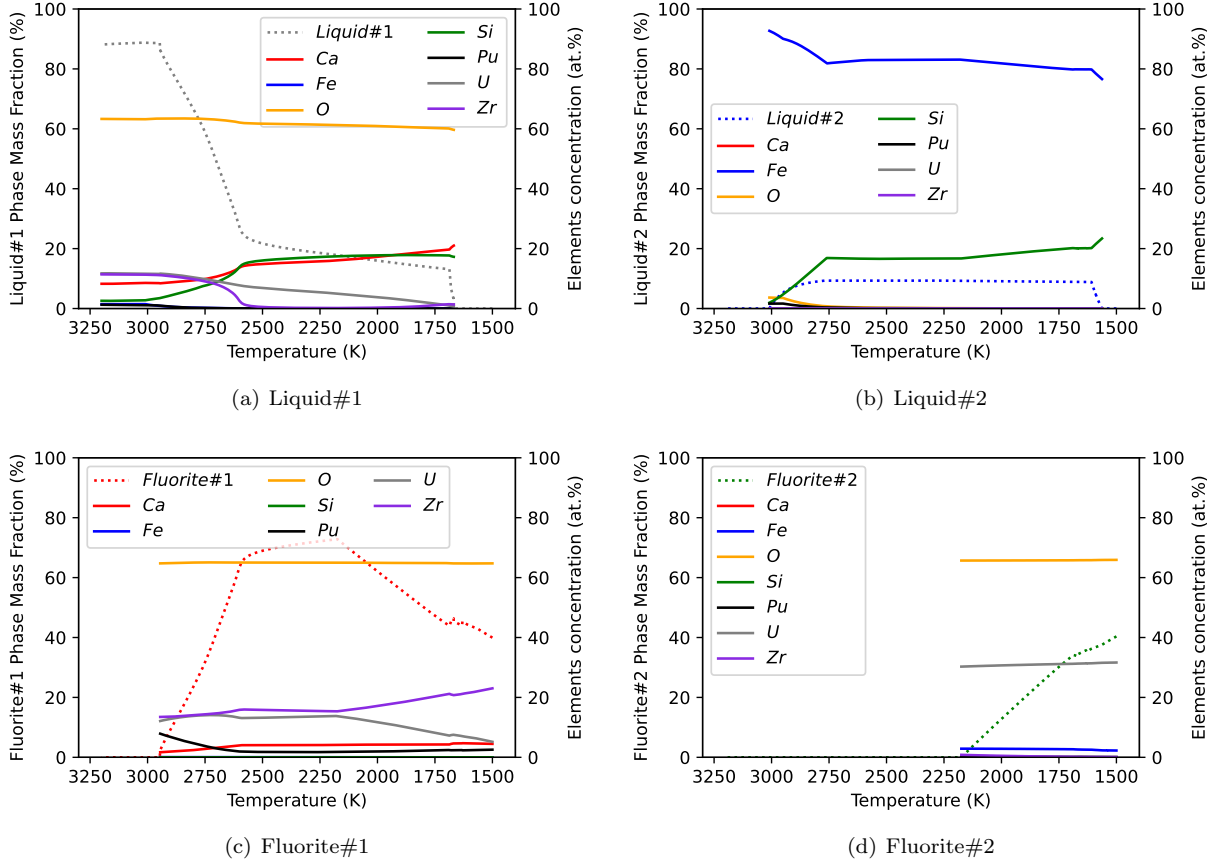


Figure 25: Calculated evolution of main phases' composition with temperature in the MOX-corium system. Dotted lines represent the mass phase fraction of the phase, while the solid lines represent the element's concentration in at.%.

Table 10: Comparison of the experimentally measured and calculated composition at 1873 K of phases in as-sintered MOX-corium.

	Phase	Composition (at.%)						
		O	Si	Ca	Fe	Zr	U	Pu
SEM-EDS	Fluorite	65.2 ± 0.0	3.7 ± 0.6	3.8 ± 0.1	0.4 ± 0.1	11.7 ± 0.7	12.8 ± 0.3	2.3 ± 0.0
	CaSiO <sub>X</sub>	61.0 ± 0.4	19.8 ± 0.6	15.5 ± 0.5	1.6 ± 0.9	0.5 ± 0.1	1.0 ± 0.2	0.6 ± 0.1
	α - Fe	0.0 ± 0.0	19.0 ± 0.4	0.0 ± 0.0	81.0 ± 0.4	0.0 ± 0.0	0.0 ± 0.0	0.0 ± 0.0
TAF-ID	Liquid#1 (α - Fe)	0.0	19.0	0.0	81.0	0.0	0.0	0.0
	Liquid#2 (CaSiO <sub>X</sub> )	60.6	17.9	18.2	0.0	0.5	2.8	0.0
	Fluorite#1	64.9	0.0	4.3	0.0	18.6	10.0	2.1
	Fluorite#2	65.7	0.0	0.0	2.8	0.3	30.9	0.2

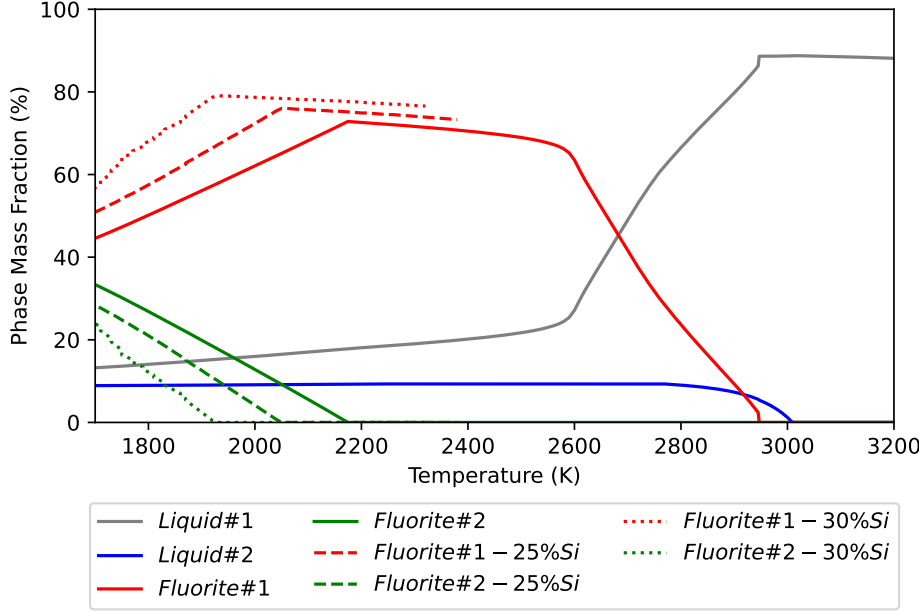


Figure 26: Sensitivity analysis of the effect of the oxygen content in the system on the temperature at which the miscibility gap in the fluorite phase is observed: the lower the oxygen chemical potential (and higher Si content in the metallic phase) the lower the miscibility gap temperature.

#### Laser Heating on MOX-corium.

The experimental and calculated liquidus and solidus temperatures in the MOX-corium system are presented in Table 11. As observed, there is approximately a 200 K difference between the calculated and measured liquidus temperature, and approximately 100 K between the calculated and measured solidus temperatures. There is, however, a considerable uncertainty on the liquidus temperature determined experimentally in this system, as already discussed in the corresponding section. Calculations indicate that the gas phase in this system is stable above 2758 K, caused by the increased volatility of Si species at a  $\mu O_2$  lower than that of the UO<sub>2</sub>-corium system. It is possible that this gas phase would have interfered with the laser measurements or even the solidification behaviour of the system. Indeed, it was observed during laser heating experiments that the RLS, which gives information on the surface of the molten material, presented multiple oscillations even during the solidification stage. Further experimentation at a hydrostatic pressure high enough to suppress the formation of the gas phase would be required to properly determine the liquidus temperature. Despite these limitations, experimental observations indicate that the solidus temperature of the MOX-corium system is 2684 K, or 241 K higher than in UO<sub>2</sub>-corium. The TAF-ID reproduces this trend, as the solidification temperature in the MOX-corium system is calculated to be 176 K higher than in the UO<sub>2</sub>-corium one. The difference between calculations and experimental observations can be attributed, in part, to the thermodynamic models (notably the U-Pu-Zr-O and Fe-Si-O), or to the fact that the calculated solidus temperature is estimated as the temperature at which the fraction of fluorite stabilizes. The higher solidus temperature in the MOX-corium system is, according to the TAF-ID, mainly a result of the lower oxygen content than of the presence of Pu.

SEM-EDS analyses on the melted region indicate a depletion of Si both in the metallic and CaSiO<sub>X</sub> phases,

along with a reduction in the number of metallic precipitates. Although during laser heating experiments it was observed that the sample consumed oxygen from the carrier gas, no evidence of Fe oxidation was observed experimentally. TAF-ID calculations can also help interpret this behaviour. Indeed, as observed in Figure 27, the Si content in the metallic liquid phase at 2600 K decreases as the  $\mu_{O_2}$  increases. In addition, the calculated main components of the gas phase are  $Fe_{(g)}$  and  $SiO_{(g)}$ . Then, oxygen consumption can be explained by the oxidation of Si in the metallic phase, and its depletion in the metallic and  $CaSiO_x$  phases by the release of  $SiO_{(g)}$ .

Table 11: Experimental and calculated Liquidus and Solidus temperatures in the MOX-corium system.

	<b>Experimental (K)</b>	<b>Calculated (K)</b>
Liquidus	$2751 \pm 26$	2947
Solidus	$2684 \pm 5$	2590

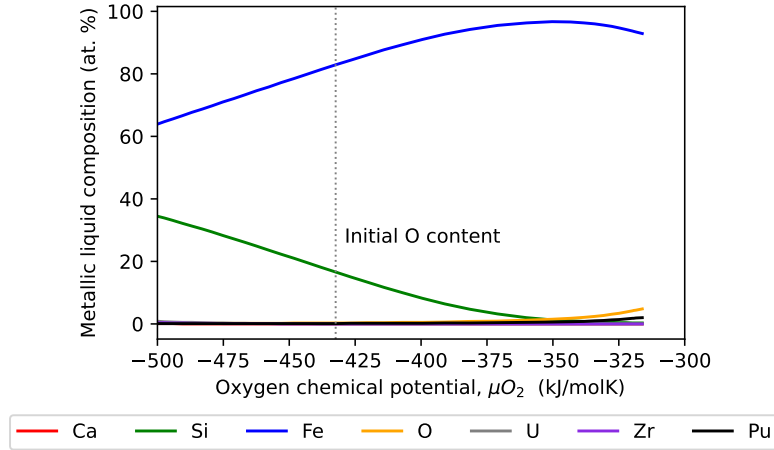


Figure 27: Evolution of the metallic liquid composition with increasing oxygen chemical potential,  $\mu_{O_2}$ , at 2600 K. As the  $\mu_{O_2}$  increases, Si is oxidized and its concentration in the metallic liquid decreases, in good agreement with experimental observations.

#### 4. MOX-Lanthanides

Experimental observations completed on the MOX-Lanthanide (MOX-Ln) system include EPMA and XRD (both only on as-sintered material), laser heating, and KEMS. These results are presented next, followed by a comparison to thermodynamic calculations. Unless specified, MOX-Ln refers to the hypo-stoichiometric sample ( $O/M=1.97$ ). As a reminder, the sintering temperature (1873 K) could not be maintained for both the stoichiometric and hypo-stoichiometric samples due to technical problems, resulting in a natural cool-down after reaching the target temperature.

#### 4.1. Experimental results

##### 4.1.1. EPMA characterisation

A Back-Scattered Electron (BSE) image acquired at the centre of a MOX-Ln sample is presented in Figure 28. Characterisations completed on the sample indicate the presence of an unexpected Si-rich phase, highlighted in Figure 28 (right), in which Pu and lanthanides (particularly La and Ce) are dissolved. The latter phase likely originated from a Si contamination during the sample fabrication process. Image analysis indicates that the fraction of the area occupied by this Si-rich phase is on average 3.9 %, although in some regions of the sample it increased up to 8.8 %. Two other phases have also been identified besides the Si-rich one: a fluorite phase (crystal structure confirmed by XRD) that constitutes the matrix of the sample and a second phase with a composition similar to the fluorite matrix but depleted in Pu. Additionally, the second Pu-depleted phase was observed exclusively surrounding pores where the fraction of Si-rich contaminant is high. This distribution of phases can be observed on the BSE image and Pu-X-ray map presented in Figure 29. The points highlighted on the latter indicate the three different phases:

- (i) the Si-rich phase is highlighted by blue x marks, which correspond to the dark grey regions on the BSE image (depleted in uranium) and at the same time to the bright (yellow) regions on the Pu X-ray map;
- (ii) the Fluorite#1 phase, which constitutes the matrix of the sample, is highlighted by red x marks; and
- (iii) the green x marks correspond to the the Pu-depleted phase (darker green on the Pu X-ray map; likely a fluorite phase as well, Fluorite#2).

The quantitative measurements included in Figure 29 correspond to the average composition of the three highlighted phases but considering all the measurements on the sample, along with the standard deviation of the considered data. Since oxygen is a light element and X-ray techniques such as EPMA and SEM are not sensitive enough, the indicated standard deviation considers a  $\pm 5\%$  uncertainty in the measured concentration. Values in at.% were calculated from the normalized wt.% ones, also included for reference. These measurements indicate that Ce, La, and Pu have a particular affinity for the Si-rich phase, being the ratio of elements consistent with  $M_2SiO_4$  ( $M=$ metal).

Despite the Si contamination of these samples, it was decided to continue with the experimental plan since (i) manufacturing a new sample would considerably delay the project (which was already delayed by the COVID-19 outbreak disruption) and (ii) meaningful data would still be obtained as Si is present in the TAF-ID but the interactions of this element with lanthanides has not been studied.

***Note to the reader: ICP-MS characterisation of a sample will be conducted at JRC during the summer, to accurately quantify the Si content. Results will be included in this report.***

##### 4.1.2. XRD characterisation

The diffractogram collected on the MOX-Ln sample is presented in Figure 30, along with that of the stoichiometric sample ( $O/M=2.00$ ). Both diffractograms have been normalized to the intensity of the most

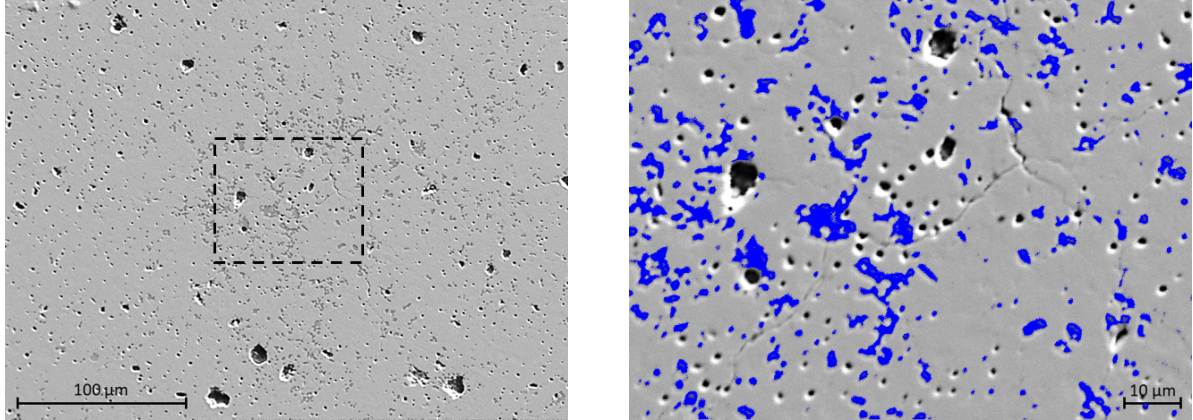
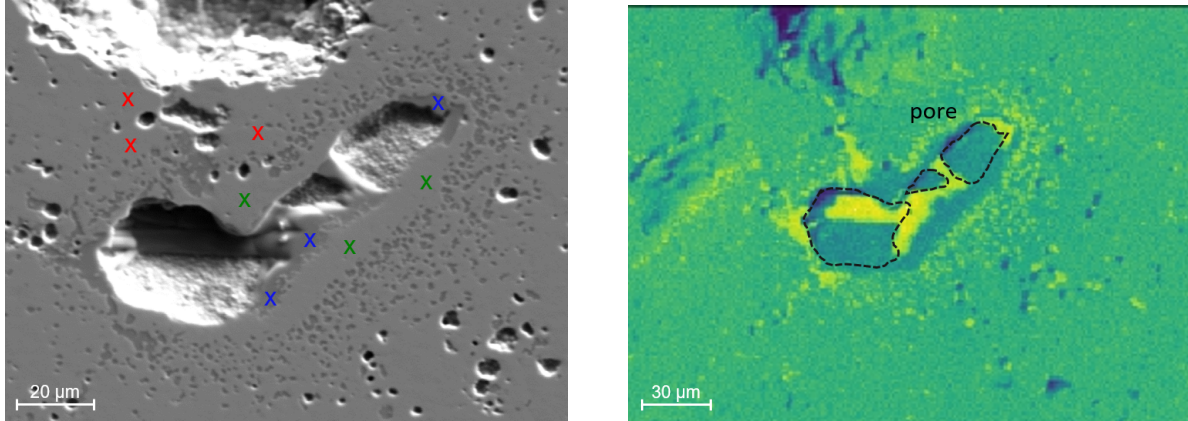


Figure 28: EPMA-BSE image of the centre of a MOX-Ln sample (left), highlighting the presence of the  $M_2SiO_4$  secondary phase ( $M=Pu$ , Ce, Gd, La, Nd, right). The area fraction of this secondary phase is 3.9 % (left), but in some regions of the sample it can be as high as 8.8% (right).

intense peak (peak (1 1 1) of the fluorite structure). Details of the differences between the stoichiometric and hypo-stoichiometric samples (top right) and of secondary phases (bottom right) are also included. The refined lattice parameters of both structures is presented in Table 6. The difference in the relative intensity of peaks between samples, observed in Figure 30, is attributed to a preferred orientation of crystals caused either by the small amount of sample used in characterisations or to the sample holder being static during measurements. As observed, the fluorite structure diffraction lines in the hypo-stoichiometric sample are shifted to lower angles compared to those of the stoichiometric one. The refined lattice parameters of the fluorite phase are 5.447 and 5.454 Å in the stoichiometric and hypo-stoichiometric samples, respectively. This shift towards lower angles can be attributed to the hypo-stoichiometry of the sample. Indeed, it has been reported in the literature that the lattice parameter of the  $UO_2$  fluorite structure tends to increase as the O/M ratio decreases [14]. The broadening of peaks from the hypo-stoichiometric sample can be attributed to (i) a non-equilibrium situation, or (ii) the presence of a second fluorite phase. In the first case, the O/M of the material at the periphery of the sample would be lower than that at the centre due to the low sintering time (the targeted sintering temperature was not held). In the second case, the different composition of the fluorite phases (higher U and lower Pu content in Fluorite#2) would result in different lattice parameter. However, the observed phase fraction of the Pu-depleted Fluorite#2 phase alone is likely too low to produce such a pronounced broadening of peaks. The peaks highlighted on bottom-right frame in Figure 30 correspond to a phase other than a fluorite, likely the  $M_2SiO_4$  phase observed in the samples. The structure of this phase, however, could not be identified as it does not match any of the available reference structures:  $SiO_2$ -quartz,  $SiO_2$ -tridymite,  $La_{1.56}SiO_{4.33}$ -hexagonal, rankinite ( $Ca_3Si_2O_7$ , monoclinic). There is no further data reported in the literature describing Si-Lanthanide (Ln)-O phases with Si/Ln/O ratios similar to those measured in these samples.

#### 4.1.3. Laser Heating

The thermogram and RLS recorded during the 1<sup>st</sup> and 5<sup>th</sup> laser shots on a MOX-Ln sample are presented in Figure 31. This sample behaved differently to the ex-vessel corium samples: during the cooldown stage,



Phase	Composition (at.%)								O/M
	U	Pu	O*	La	Ce	Nd	Gd	Si	
M <sub>2</sub> SiO <sub>4</sub>	2.1 ± 1.7	7.3 ± 0.4	60.9 ± 1.0	6.8 ± 0.6	4.2 ± 0.3	3.0 ± 0.2	2.1 ± 0.2	13.6 ± 0.8	1.56
Fluorite#1	25.9 ± 0.3	6.1 ± 0.1	64.8 ± 0.3	0.8 ± 0.1	0.8 ± 0.1	0.8 ± 0.1	0.9 ± 0.1	-	1.84
Fluorite#2	29.0 ± 0.4	4.4 ± 0.2	65.0 ± 0.2	0.3 ± 0.1	0.4 ± 0.1	0.5 ± 0.1	0.6 ± 0.1	-	1.86
Composition (wt.%)									
M <sub>2</sub> SiO <sub>4</sub>	8.3 ± 6.9	29.7 ± 1.5	16.3 ± 0.5	15.8 ± 1.3	9.8 ± 0.8	7.2 ± 0.6	5.6 ± 0.4	6.4 ± 0.4	99.1 ± 2.2
Fluorite#1	66.2 ± 0.5	15.9 ± 0.3	11.1 ± 0.1	1.2 ± 0.1	1.2 ± 0.1	1.3 ± 0.1	1.5 ± 0.1	-	98.4 ± 0.2
Fluorite#2	73.6 ± 0.7	11.4 ± 0.5	11.1 ± 0.1	0.4 ± 0.1	0.5 ± 0.1	0.7 ± 0.1	1.0 ± 0.1	-	98.7 ± 0.1

Figure 29: Left: EPMA-BSE image of a pore in a MOX-Ln sample. The highlighted points correspond to quantitative analyses on the three identified phases: the M<sub>2</sub>SiO<sub>4</sub> phase, Fluorite#1, and Fluorite#2. Right: Pu X-ray map showing that the Fluorite#2 phase, depleted in Pu, is found mainly surrounding pores along with important quantities of the M<sub>2</sub>SiO<sub>4</sub> phase. Yellow colour indicates high Pu concentration, dark green low Pu concentration. \*Oxygen is a light element and its concentration could be up to ±5% off, due to limitations of the EPMA.

Table 12: Refined lattice parameters of the fluorite structure identified in stoichiometric and hypo-stoichiometric MOX-Ln samples.

Sample (O/M)	Fluorite lattice parameter (a, Å)	
	Refined	Reference: UO <sub>2</sub>
MOX-Ln (2.00)	5.447	5.473
MOX-Ln (1.97)	5.454	

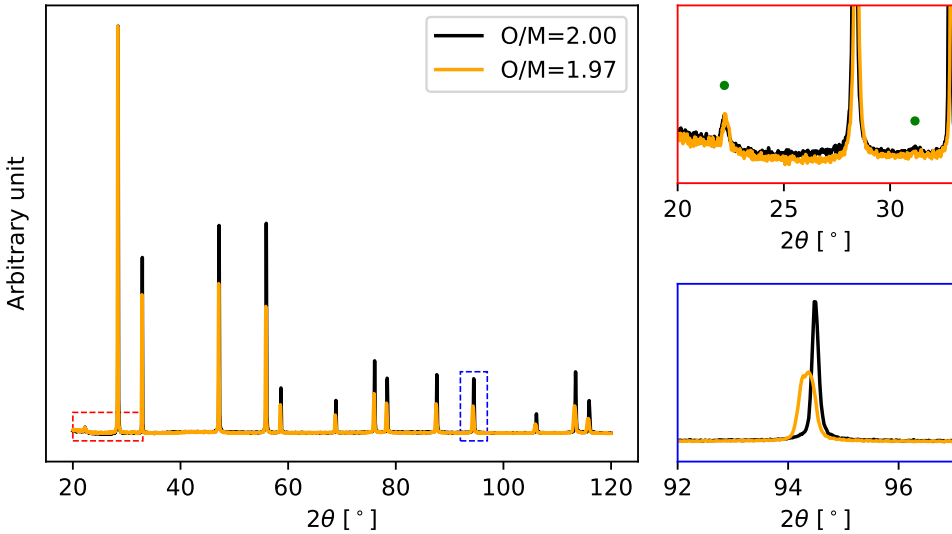


Figure 30: XRD characterisation of stoichiometric (black) and hypo-stoichiometric (orange) MOX-Ln samples. The peaks highlighted in the top-right frame would correspond to the  $M_2SiO_4$  phase, otherwise, a single fluorite was observed in both samples. In the hypo-stoichiometric sample, the fluorite diffraction lines are shifted to lower angles and are broader (bottom-right frame). The broadening could be caused by the miscibility gap observed by EPMA or to an oxygen gradient in the sample due to the low sintering time.

temperature decreased below the maximum temperature measured during thermal arrest, in a behaviour called supercooling. This behaviour is usually exhibited either by pure materials, which lack of crystallization nuclei, or by liquids with a high cooldown rate. Although the latter is the most likely reason for this behaviour, the cooling rate should have been similar to that of ex-vessel corium samples (same experimental set-up), which did not exhibit supercooling. However, a similar behaviour has been observed in the past on related chemical systems and similar experimental set-up (*e.g.*, U-Am mixed oxides [15] and U-Pu mixed oxides [10, 16]). In these works, the solidus temperature was considered to be the maximum temperature observed during the thermal arrest. As with ex-vessel corium samples, the liquidus temperature was determined as the first inflection point on the thermogram, before the thermal arrest. It must be considered though that there is limited information available on such complex systems and this approach might not be appropriate. In any case, the liquidus and solidus temperatures measured over five successive laser shots in a MOX-Ln sample are presented in Table 13. The average liquidus temperature was  $3106 \pm 29$ , while the solidus one

was  $3039 \pm 27$  K. Both temperatures showed the tendency to increase after each melting sequence. This temperature increase can be attributed to the release of volatile Si-species, with the sample behaviour shifting towards that of a non-contaminated material (refer to TAF-ID calculations in section 4.2).

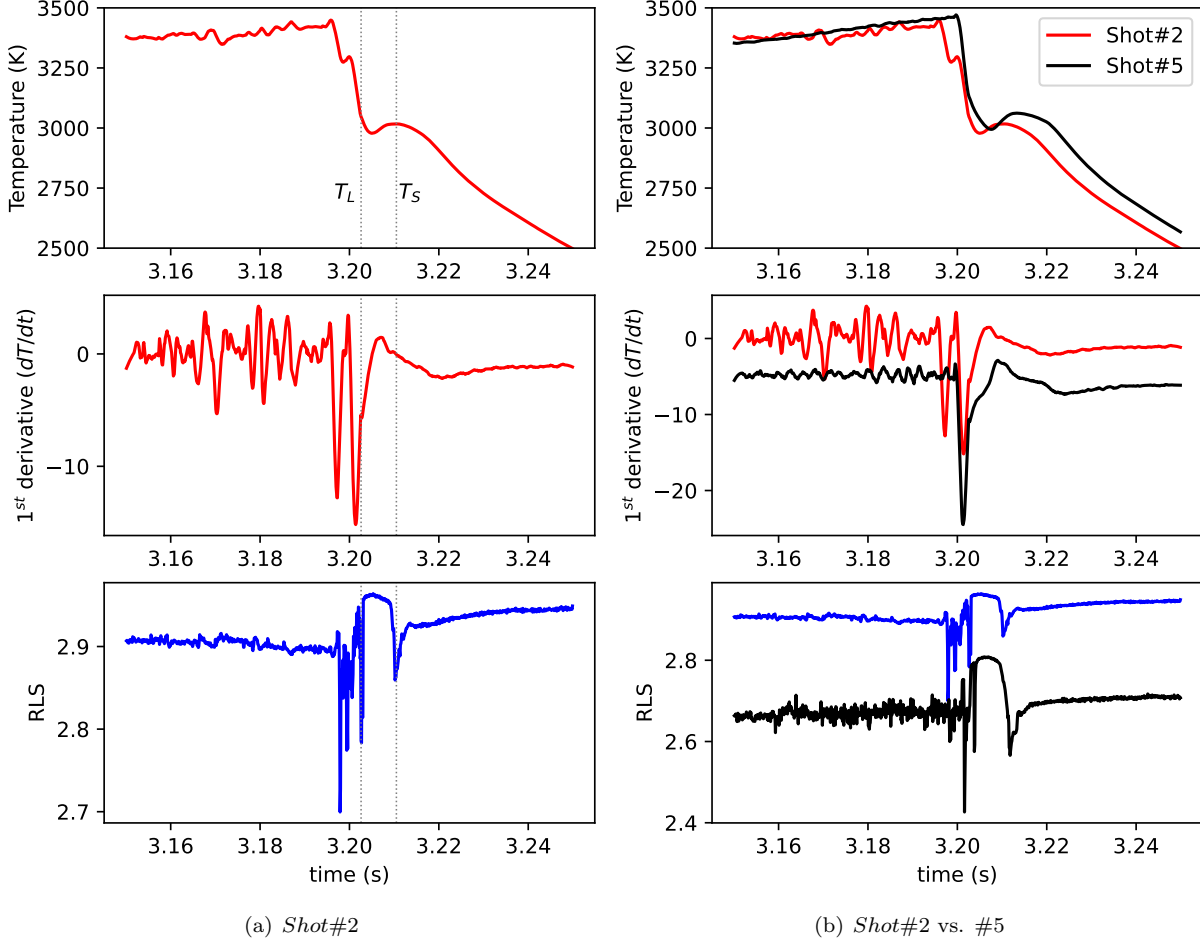


Figure 31: Left: Thermogram, its  $1^{st}$  derivative, and RLS signal acquired during the  $2^{nd}$  laser shot on a hypo-stoichiometric MOX-Ln sample. This sample exhibited super cooling: the temperature dropped below the solidification temperature,  $T_S$  (associated to the maximum temperature of the thermal arrest). The liquidus temperature,  $T_L$ , would correspond to the feature observed on the  $1^{st}$  derivative of the thermogram. Right: Comparison of results acquired during the  $2^{nd}$  and  $5^{th}$  laser shots on the same sample. Liquidus and solidus temperatures increased after each melting sequence. The  $1^{st}$  derivative and RLS data for Shot#5 are shifted vertically for ease of comparison.

#### 4.1.4. Knudsen Effusion Mass Spectrometry (KEMS)

Experimental and calculated vapour pressures of  $\text{UO}_X$  (top) and  $\text{PuO}_X$  (bottom) species are presented in Figure 32, considering the nominal composition of the system ( $\text{O/M}=1.97$ ) with 1 wt.% Si contamination (left) and pure, stoichiometric materials with no Si contamination (right). As observed, the agreement between calculations and experiments for the hypo- and stoichiometric phases is not consistent between  $\text{UO}_X$  and  $\text{PuO}_X$  species:  $\text{UO}_X$  species behaviour would correspond to non-contaminated stoichiometric material, while that of  $\text{PuO}_X$  species is more in agreement with the hypo-stoichiometric, contaminated

Table 13: Liquidus ( $T_L$ ) and Solidus ( $T_S$ ) temperatures measured in a hypo-stoichiometric MOX-Ln sample by laser heating. Experimental error:  $\pm 2\%$ .

	Emissivity	$T_L$ (K)	$T_S$ (K)
Shot#1	0.75	-	2992
Shot#2	0.75	3048	3017
Shot#3	0.75	3122	3059
Shot#4	0.75	3135	3062
Shot#5	0.75	3121	3063
Average	0.75	$3106 \pm 29$	$3039 \pm 27$

one. The latter agreement, however, is worse than in ex-vessel corium samples. This dissimilar behaviour between species can be attributed to a combination of two reasons: (i) the O/M ratio that was determined by thermogravimetry might not be representative of the actual oxygen content of the sample (as the Si-contamination was not accounted for) and (ii), the TAF-ID fails to reproduce the behaviour of Pu species as the Pu-Si-O system is not yet assessed in the database.

#### 4.2. TAF-ID Calculations

The calculated phases in equilibrium with decreasing temperature for the hypo-stoichiometric MOX-Ln system are presented in Figure 33. The two diagrams correspond to the system with silicon contamination (left, considering a Si content in the sample of 1 wt.%) and without (right), for comparison purposes. The evolution of phase composition in the Si-contaminated system is presented in Figure 34. According to calculations, a single liquid exist at high temperature ( $T > 2800$  K). This liquid solidifies between 2907 (liquidus) and 1651 K (solidus). Small quantities of Pu and Ce are present in the liquid (1.7 at.% each at 1873 K), as observed in Figure 34 (a) but, once the liquid solidifies only pure  $\text{SiO}_2$  compounds are calculated. This is just a consequence of missing thermodynamic assessments for the systems Si-Pu-O, Si-Ce-O, Si-Gd-O, Si-La-O, and Si-Nd-O in the TAF-ID. A single fluorite is produced during the solidification of the liquid phase, although a miscibility gap below 1473 K leads to the formation of a second fluorite phase. As observed in Figure 34 (b) and (c), the main difference between these fluorite phases is the Pu/lanthanides content, being the initial Fluorite#1 richer in Pu (consistently above 6 at.% Pu in the considered temperature range) and Fluorite#2 richer in Nd (Pu content < 3.0 at.%, Nd > 1.8 at.%). According to calculations, the presence of Si does not affect the fluorite miscibility gap, although this could also be a consequence of the missing thermodynamic assessments.

#### 4.3. Comparison of Experimental and Calculation Results

##### As-sintered MOX-Ln

Three phases were observed experimentally in the hypo-stoichiometric MOX-Ln sample sintered at 1873 K: a first fluorite phase (#1) that constitutes the matrix of the sample, a second fluorite phase (#2) but with a lower Pu content, and a Si, Pu, and Lanthanides-rich phase denoted as  $\text{M}_2\text{SiO}_4$ , which

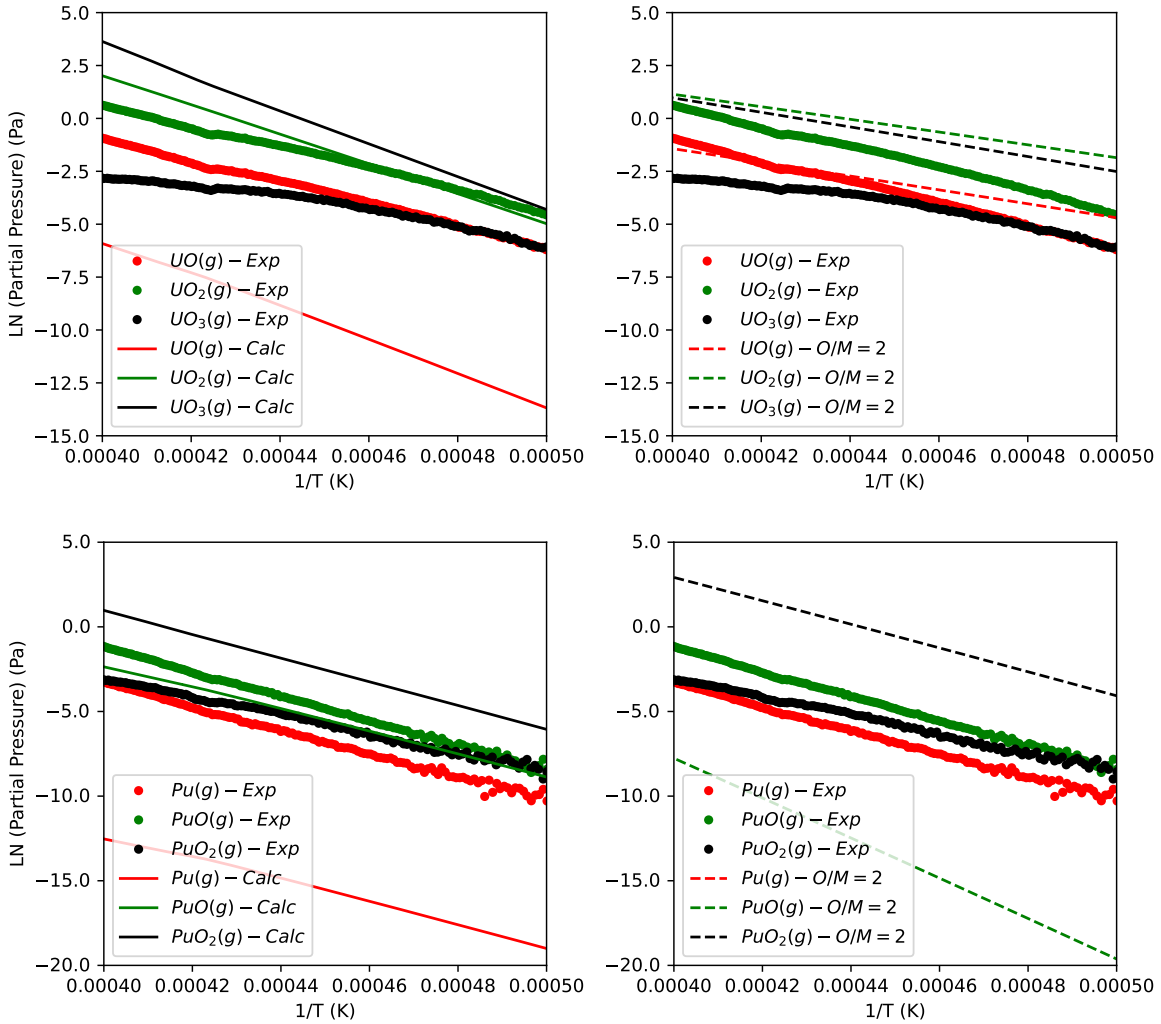


Figure 32: Vapour pressure of  $UO_X$  and  $PuO_X$  species in hypo-stoichiometric MOX-Ln, determined by KEMS. Results are compared to thermodynamic calculations considering  $O/M=1.97$  (left) and to pure stoichiometric phases (stoichiometric  $UO_2$  and  $PuO_2$  with no lanthanides) (right).

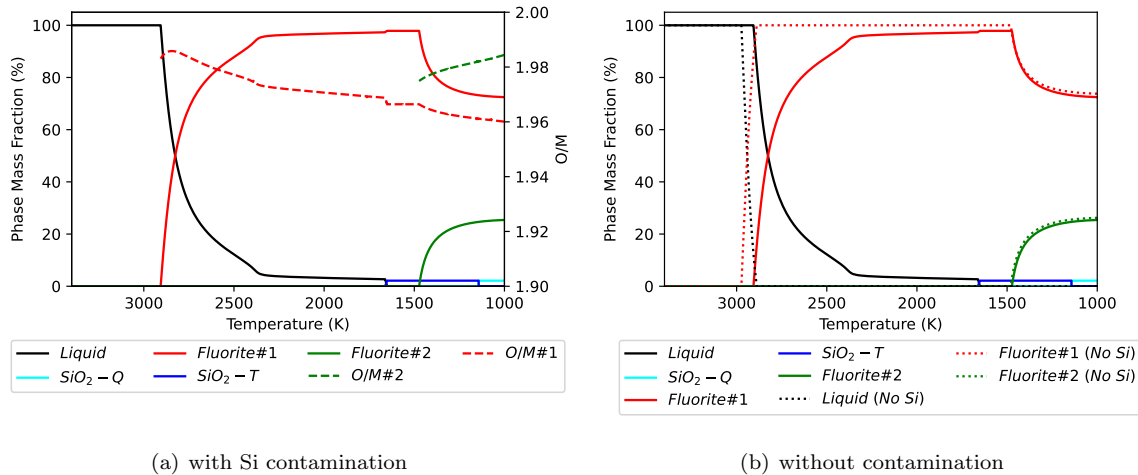


Figure 33: Calculated phases in equilibrium with decreasing temperature in the hypo-stoichiometric MOX-Ln sample. Left: calculations considered 1 wt.% Si contamination. Right: Comparison of calculations with and without (dotted lines) Si contamination.  $\text{SiO}_2\text{-Q}$  and  $\text{SiO}_2\text{-T}$  refer to the Quartz and Tridymite structures, respectively.

is likely a consequence of Si contamination during the samples fabrication process. Regarding calculations, the TAF-ID predicts a Si-rich liquid phase with a low Pu and Ce content at the sintering temperature. No Si/Pu/lanthanides solid phases are calculated however, as there are no thermodynamic models in the database for these systems. Lastly, the TAF-ID does calculate the miscibility gap in the fluorite phase, but only below 1473 K. Possible reasons for the presence of the Fluorite#2 phase 400 K above the calculated miscibility gap temperature are (i) the thermodynamic model is not accurate, (ii) the system was not in thermodynamic equilibrium, and (iii) the presence of Si can somehow stabilize the Fluorite#2. The system not being in thermodynamic equilibrium can be explained by the short sintering time: as a reminder, the furnace did not hold 1873 K for 4 hours, but stopped immediately after reaching the target temperature and cooled down naturally. A second MOX-Ln sample was annealed at 1400 K for 48 hours, in an attempt to increase the fraction of Fluorite#2, but no difference was observed either on the phases fraction or in their composition. The measured and calculated composition of these phases is presented in Table 14. In the latter, the composition of the Fluorite#1 and  $M_2SiO_4$  phases were calculated at the sintering temperature (1873 K), while that of the Fluorite#2 phase was calculated at 1400 K. The disagreement between measured and calculated composition of the phases is expected due to the reasons already mentioned (*i.e.*, system not in thermodynamic equilibrium, missing thermodynamic models in the database). As a reminder, the EPMA measured concentrations are the average of all the measurements on this sample and the value ranges correspond to the standard deviation of results.

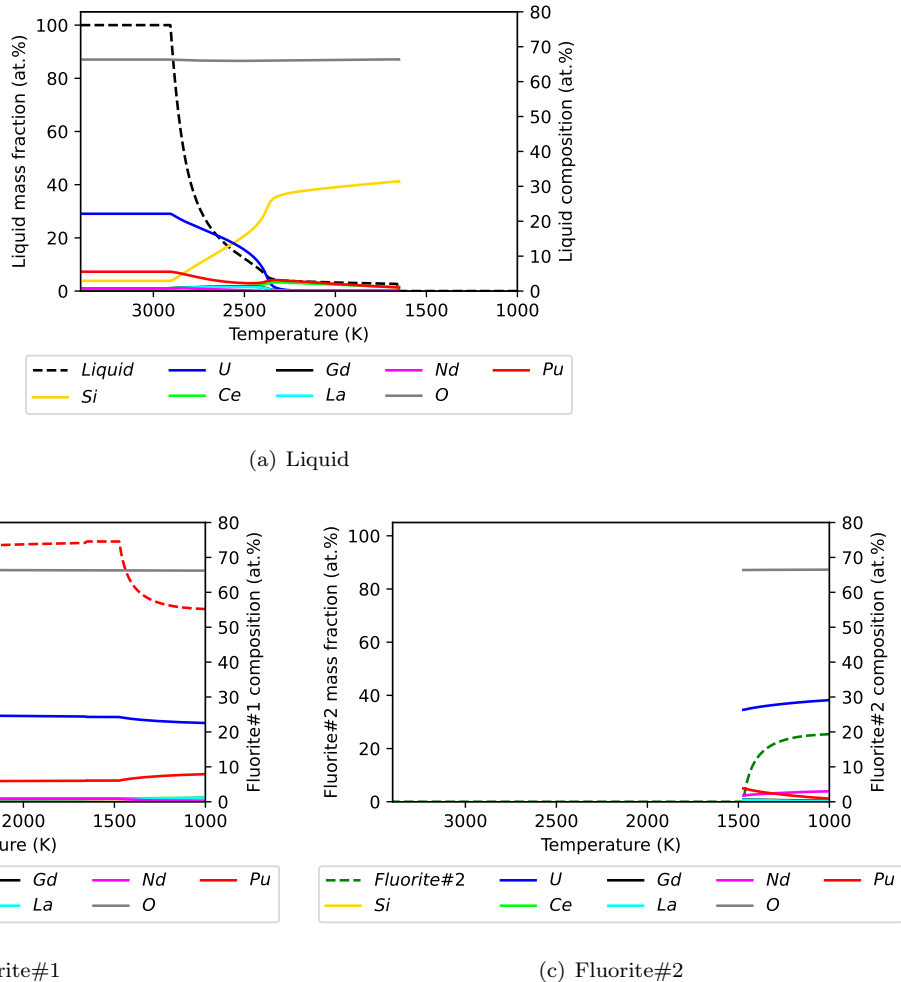


Figure 34: Calculated evolution of main phases composition vs. temperature for a hypo-stoichiometric MOX-Ln system.

Table 14: Comparison of the experimentally measured and calculated composition of phases in as-sintered MOX-Ln.

	Phase	Composition (at.%)								
		U	Pu	O	La	Ce	Nd	Gd	Si	O/M
EPMA	M <sub>2</sub> SiO <sub>4</sub>	2.1 ± 1.7	7.3 ± 0.4	60.9 ± 1.0	6.8 ± 0.6	4.2 ± 0.3	3.0 ± 0.2	2.1 ± 0.2	13.6 ± 0.8	1.56
	Fluorite#1	25.9 ± 0.3	6.1 ± 0.1	64.8 ± 0.3	0.8 ± 0.1	0.8 ± 0.1	0.8 ± 0.1	0.9 ± 0.1	-	1.84
	Fluorite#2	29.0 ± 0.4	4.4 ± 0.2	65.0 ± 0.2	0.3 ± 0.1	0.4 ± 0.1	0.5 ± 0.1	0.6 ± 0.1	-	1.86
TAF-ID	M <sub>2</sub> SiO <sub>4</sub>	0.0	1.6	66.3	0.0	1.6	0.0	0.1	30.4	1.96
	Fluorite#1	24.5	6.0	66.3	0.8	0.7	0.9	0.8	-	1.97
	Fluorite#2*	28.5	1.5	66.5	0.3	0.1	2.8	0.4	-	1.98

\*Calculated at 1400 K.

### Laser Heating experiments

The liquidus and solidus temperatures measured experimentally over five laser heating sequences are on average  $3106 \pm 29$  and  $3039 \pm 27$  K, respectively. Considering Si contamination (Figure 33 (a)), the TAF-ID predicts a liquidus at 2906 K. Determining the solidus in this system is not as straightforward. Strictly speaking, it should be considered as the temperature at which the liquid phase is fully solidified. However, by taking a similar approach as with the MOX-corium sample, the solidus can be considered as the temperature at which the phase fraction of the Fluorite#1 (matrix of the sample) does not evolve considerably as temperature decreases. With this consideration, the solidus of the system is estimated to be 2360 K, which is 680 K below the temperature measured experimentally. It is not possible to draw any meaningful conclusion from such a large disagreement as there are many factors that may affect the solidification behaviour or calculations results, and are likely not accounted for. Some of these factors are:

- (i) Missing thermodynamic models for Si-M-O systems in the database, where M= Pu, Ce, Gd, La, Nd.
- (ii) The uncertainty on the oxygen content of the sample. The O/M ratio in the hypo-stoichiometric MOX-Ln sample was determined by thermogravimetry without considering silicon contamination. As observed with ex-vessel corium samples, the oxygen content has a major impact on the liquidus and solidus temperatures of the material.
- (iii) The effect of Si-species release at high temperature. Experiments on ex-vessel corium samples highlighted the volatility of Si species but, since their release cannot be quantified, the impact on the solidification behaviour of the samples cannot be estimated.

The release of Si-species could explain the observed increase of the liquidus and solidus temperatures after each laser heating sequence. Indeed, the release of volatile Si-species would reduce the contamination of the system, bringing its behaviour closer to that of the Si-free system presented in Figure 33 (b). In the latter case, the calculated liquidus and solidus temperature are 2974 and 2888 K, respectively. The measured and calculated liquidus and solidus temperatures are summarized in Table 15.

Table 15: Experimental and calculated solidus and liquidus temperatures for a hypo-stoichiometric MOX-Ln system. Calculations consider a Si-contaminated (with 1 wt.% Si) and a Si-free systems.

	Experimental (K)	Calculated (K)	
		Si-contaminated	Si-free
Liquidus	$3106 \pm 29$	2906	2974
Solidus	$3039 \pm 27$	2360	2888

## 5. Conclusions and recommendations

### 5.1. Ex-vessel corium samples

The objective of this report is to summarize experimental observations done at JRC-Karlsruhe and thermodynamic calculations using the TAF-ID. Therefore, experimental results have not been thoroughly

compared to other similar experimental work available in the litterature. TAF-ID calculations on these systems were generally in good agreement with experimental observations, particularly for the UO<sub>2</sub>-system. Indeed, the number and type of phases and the solidus and liquidus temperatures were all accurately predicted by the TAF-ID. There were differences on the formation of a miscibility gap in the fluorite phase at high temperature (solidification after laser melting experiments), and on the composition of the two fluorite phases at the sintering temperature. These differences cannot be completely dissociated from kinetic phenomena, which are independent of the quality of the thermodynamic models for the concerned systems. For instance, the rapid cooling rate ( $\approx 9000$  K/s) and the diffusion of species would have impacted the formation of the miscibility gap and the equilibration of the phase compositions. Regarding the MOX-corium system, a good agreement was also observed between the calculated vapour pressure of species and KEMS experimental results. On the other hand, significant differences were observed in the calculated and measured liquidus ( $\approx 200$  K) and solidus ( $\approx 100$  K) temperatures. This difference can be attributed in part to the presence of a gas phase at high temperature that hindered the correct determination of the liquidus temperature. Nevertheless, the TAF-ID was able to reproduce the increased solidification temperature in the MOX-corium system compared to the UO<sub>2</sub> system. Laser heating experiments at a hydrostatic pressure high enough to suppress the formation of the gas phases would allow a better determination of the liquidus temperature. The TAF-ID failed to calculate accurately the temperature at which a miscibility gap is observed in the fluorite phase: while no miscibility gap is observed experimentally in as-sintered MOX-corium (at 1873 K), the TAF-ID calculates that this gap would form already at 2174 K. This highlights the need to revise the U-Zr-O system in the database (and possibly the U-Pu-Zr-O and Si-Fe-O, being the latter the base for the oxygen content estimation in the system). Despite these limitations, the TAF-ID can help explain other phenomena observed experimentally such as the oxygen consumption at high temperature, depletion of elements due to release at high temperature, oxidation of Fe and its interaction with concrete species, etc.

### 5.2. MOX-Ln

Experimental observations on this system showed evidence of Si contamination, likely produced during the preparation of samples. This contamination led to the formation of a secondary phase containing Pu and lanthanides, in a ratio that is consistent with a M<sub>2</sub>SiO<sub>4</sub> compound (where M=Pu, Ce, Gd, La, Nd). This phase represents on average 3.9 % of the sample surface and the total Si concentration was estimated to be about 1 wt.%. As a consequence, the Si contamination modified the intended composition of the fluorite matrix of the samples. Nevertheless, experimental observations did confirm the presence of a second fluorite phase, depleted in Pu, which is predicted by the TAF-ID and was the objective of these observations. The apparent phase fraction of the second fluorite phase is low compared to thermodynamic calculations. A second annealing test at 1400 K for 48 h did not modify the ratio of fluorite phases. This was be attributed to the presence of the secondary Si-rich phase, which captured Pu and lanthanides that would otherwise induce the miscibility gap in the fluorite phase. The liquidus and solidus temperatures measured by laser heating and the vapour pressure of species measured by KEMS deviated from the thermodynamic calculations, likely due to the uncertainty on the sample oxygen content (thermogravimetric analyses did not consider the presence of the Si phase) or to missing thermodynamic assessments in the TAF-ID (Si-O-M, where M=Pu, Ce, Gd, La, Nd). Experimental results are nevertheless relevant as they have identified knowledge gaps in the database. The latter would be of most importance for calculations related to the partition of

fission products in ex-vessel corium systems. Inductively Couple Plasma - Mass Spectrometry (ICP-MS) characterisation of a MOX-Ln sample is planned in order to determine more accurately the Si content. An accurate determination of the Si content would improve the thermodynamic calculations.

## 6. References

- [1] “Private communication,” tech. rep., Japan Atomic Energy Agency, Japan, 2021.
- [2] D. Manara, L. Soldi, S. Mastromarino, K. Boboridis, D. Robba, L. Vlahovic, and R. Konings, “Laser-heating and radiance spectrometry for the study of nuclear materials in conditions simulating a nuclear power plant accident,” *JoVE (Journal of Visualized Experiments)*, no. 130, p. e54807, 2017.
- [3] M. Welland, R. Böhler, L. Vlahovic, K. Boboridis, and D. Manara, “Co-development of experimental and simulation methods for the laser flash heating and melting technique: The thermoelastic effects of  $\text{UO}_2$ ,” *International Journal of Thermal Sciences*, vol. 132, pp. 174–185, 2018.
- [4] J.-L. Pouchou and F. Pichoir, *Quantitative Analysis of Homogeneous or Stratified Microvolumes Applying the Model “PAP”*, pp. 31–75. Boston, MA: Springer US, 1991.
- [5] I. R. Farthing and C. T. Walker, “Heinrich’s mass absorption coefficients (for the k, l and m x-ray lines),” Technical Note K0290140, Commission of the European Communities, Joint Research Centre, Karlsruhe, 1990.
- [6] P. Pöml and X. Llovet, “Determination of mass attenuation coefficients of Th, U, Np, and Pu for oxygen K $\alpha$  X-Rays using an electron microprobe,” *Microscopy and Microanalysis*, vol. 26, no. 2, pp. 194–203, 2020.
- [7] A. L. Smith, J. Y. Colle, O. Beneš, A. Kovács, P. E. Raison, and R. J. M. Konings, “Mass spectrometric study of the vaporization behaviour of  $\alpha\text{-Na}_2\text{NpO}_4$ : Thermodynamic investigation of the enthalpy of formation,” *The Journal of Chemical Thermodynamics*, vol. 60, pp. 132–141, 2013.
- [8] D. Manara, M. Sheindlin, W. Heinz, and C. Ronchi, “New techniques for high-temperature melting measurements in volatile refractory materials via laser surface heating,” *Review of Scientific Instruments*, vol. 79, no. 11, p. 113901, 2008. Publisher: American Institute of Physics.
- [9] D. Basak, W. J. Boettinger, D. Josell, S. R. Coriell, J. L. McClure, S. Krishnan, and A. Cezairliyan, “Effect of heating rate and grain size on the melting behavior of the alloy Nb–47 wt.% Ti in pulse-heating experiments,” *Acta Materialia*, vol. 47, no. 11, pp. 3147–3158, 1999.
- [10] R. Böhler, M. J. Welland, D. Prieur, P. Cakir, T. Vitova, T. Pruessmann, I. Pidchenko, C. Hennig, C. Guéneau, R. J. M. Konings, and D. Manara, “Recent advances in the study of the  $\text{UO}_2\text{-PuO}_2$  phase diagram at high temperatures,” *Journal of Nuclear Materials*, vol. 448, no. 1, pp. 330–339, 2014.
- [11] L. Zhang, A. Shelyug, and A. Navrotsky, “Thermochemistry of  $\text{UO}_2\text{-ThO}_2$  and  $\text{UO}_2\text{-ZrO}_2$  fluorite solid solutions,” *The Journal of Chemical Thermodynamics*, vol. 114, pp. 48–54, 2017.

- [12] J. Zhang and F. Guyot, "Thermal equation of state of iron and Fe<sub>0.91</sub>Si<sub>0.09</sub>," *Physics and Chemistry of Minerals*, vol. 26, no. 3, pp. 206–211, 1999.
- [13] M. M. Obeid, "Crystallization of synthetic wollastonite prepared from local raw materials," *International Journal of Materials and Chemistry*, vol. 4, no. 4, pp. 79–87, 2014. Publisher: Scientific & Academic Publishing.
- [14] N. A. Javed, "Thermodynamic study of hypostoichiometric urania," *Journal of Nuclear Materials*, vol. 43, no. 3, pp. 219–224, 1972.
- [15] E. Epifano, D. Prieur, P. M. Martin, C. Guéneau, K. Dardenne, J. Rothe, T. Vitova, O. Dieste, T. Wiss, R. J. M. Konings, and D. Manara, "Melting behaviour of uranium-americium mixed oxides under different atmospheres," *The Journal of Chemical Thermodynamics*, vol. 140, p. 105896, 2020.
- [16] F. De Bruycker, K. Boboridis, R. J. M. Konings, M. Rini, R. Eloirdi, C. Guéneau, N. Dupin, and D. Manara, "On the melting behaviour of uranium/plutonium mixed dioxides with high-Pu content: A laser heating study," *Journal of Nuclear Materials*, vol. 419, no. 1, pp. 186–193, 2011.

## **GETTING IN TOUCH WITH THE EU**

### **In person**

All over the European Union there are hundreds of Europe Direct centres. You can find the address of the centre nearest you online ([european-union.europa.eu/contact-eu/meet-us\\_en](http://european-union.europa.eu/contact-eu/meet-us_en)).

### **On the phone or in writing**

Europe Direct is a service that answers your questions about the European Union. You can contact this service:

- by freephone: 00 800 6 7 8 9 10 11 (certain operators may charge for these calls),
- at the following standard number: +32 22999696,
- via the following form: [european-union.europa.eu/contact-eu/write-us\\_en](http://european-union.europa.eu/contact-eu/write-us_en).

## **FINDING INFORMATION ABOUT THE EU**

### **Online**

Information about the European Union in all the official languages of the EU is available on the Europa website ([european-union.europa.eu](http://european-union.europa.eu)).

### **EU publications**

You can view or order EU publications at [op.europa.eu/en/publications](http://op.europa.eu/en/publications). Multiple copies of free publications can be obtained by contacting Europe Direct or your local documentation centre ([european-union.europa.eu/contact-eu/meet-us\\_en](http://european-union.europa.eu/contact-eu/meet-us_en)).

### **EU law and related documents**

For access to legal information from the EU, including all EU law since 1951 in all the official language versions, go to EUR-Lex ([eur-lex.europa.eu](http://eur-lex.europa.eu)).

### **Open data from the EU**

The portal [data.europa.eu](http://data.europa.eu) provides access to open datasets from the EU institutions, bodies and agencies. These can be downloaded and reused for free, for both commercial and non-commercial purposes. The portal also provides access to a wealth of datasets from European countries.

# Science for policy

The Joint Research Centre (JRC) provides independent, evidence-based knowledge and science, supporting EU policies to positively impact society



**EU Science Hub**

[joint-research-centre.ec.europa.eu](http://joint-research-centre.ec.europa.eu)

- [@EU\\_ScienceHub](#)
- [EU Science Hub - Joint Research Centre](#)
- [EU Science, Research and Innovation](#)
- [EU Science Hub](#)
- [@eu\\_science](#)



Publications Office  
of the European Union